# Determination and comparison of demagnetization times of ferromagnetic thin films
# Towards All-optical Switching in Synthetic Ferrimagnets

Bahos, A.M.

*Award date:*
2018

Eindhoven University of Technology

Department of Applied Physics

Physics of Nanostructures

# Determination and comparison of demagnetization times of ferromagnetic thin films

*Towards All-optical Switching in Synthetic Ferrimagnets*

A.M. Bahos

March, 2018

Supervisors
prof. dr. B. Koopmans
ir. M.J.G. Peeters

**Abstract**

As the writing rate of current magnetic data storage technology is nearing its limit, several solutions have been proposed in an attempt to circumvent this. One promising solution is using all-optical magnetization switching. The use of this, completely by heat driven phenomenon facilitates direct opto-magnetic conversion of data thus removing the necessity for the conventional electro-magnetic conversion, hence lowering the bound on the writing rate to picoseconds. The ultimate goal of the project is to fabricate a synthetic ferrimagnet showing single-shot all-optical magnetization switching without using gadolinium, as this material is not suitable for high density storage. In order to enable single-shot switching the ferromagnetic layers require having a distinct demagnetization time while also being coupled antiferromagnetically. In an attempt to find a suitable ferromagnetic pair, several ferromagnetic thin films were deposited by means of a DC sputtering process: $Ta_{4.0\,nm}/Pt_{4.0}/\mathbf{Co}_{0.4}/Pt_{4.0}$, $Ta_{4.0}/Pt_{4.0}/\mathbf{Co}_{0.3}/\mathbf{Ni}_{0.6}/\mathbf{Co}_{0.3}/Pt_{4.0}$, $Ta_{4.0}$ $/Pt_{4.0}$ $/\mathbf{Co}_{0.3}/\mathbf{Fe}_{0.6}/\mathbf{Co}_{0.3}$ $/Pt_{4.0}$, and $Ta_{4.0}/Pt_{4.0}/\mathbf{Co}_{0.3}/\mathbf{Fe}_{0.2}/\mathbf{Co}_{0.3}$ $/Pt_{4.0}$. Static MOKE measurements were thereafter performed in order to determine whether their magnetization was directed out-of-plane, the desired direction. This was the case for all thin films except for the $\mathbf{Co/Fe}_{0.6}$ sample. Next, time-resolved MOKE was performed on the samples with out-of-plane magnetization in order to determine their demagnetization times as a function of laser fluence. From these measurements it was concluded that the difference in demagnetization time was the largest for the **Co** and **Co/Ni** samples. More specifically, the difference was less than a factor two for a fluence of $\sim 10\,mJ/cm^2$. Unfortunately, this difference in demagnetization times is considered as being insufficient if compared to the factor ten difference in demagnetization times shown in theoretical literature. More research is thus necessary in order to find suitable ferromagnetic materials for a synthetic ferrimagnet enabling single-shot all-optical switching.

# Contents

# Chapter 1

# Introduction

*In this chapter, first, background information will be presented in an attempt to clarify the incentives for doing the project as described later on. Thereafter RKKY coupling is introduced as this interaction plays a major role in all-optical magnetization reversal in synthetic ferrimagnets. The introduction continues with a project description and ends with a thesis outline.*

## 1.1 The speed limit of current data storage technology

Since the introduction of magnetic data storage devices by IBM in 1956 [1] the boundaries of nanotechnology have been continuously pushed in order to improve their performance. The importance of this ongoing improvement is represented by a 50 billion U.S. dollar magnetic storage industry (est. for 2019 [2]). Of all magnetic storage devices *hard-disk drives* (HDDs) are the most widely used. These devices store information by changing the magnetization direction of small magnetic domains on a magnetic disk by a strong locally induced magnetic field. Until the mid 2000s the bits were written by directing the magnetization parallel to the disk plane. This way of writing HDDs is called *longitudinal magnetic recording* (LMR). From the mid 2000s onwards, due to technological developments, the magnetic recording technology was improved with the introduction of *perpendicular magnetic recording* (PMR) [3]. Since then the data bits, i.e. the 1s and 0s, have been represented by the up- and downward magnetization direction of the magnetic domains. Unfortunately, the current PMR technology is nearing its limit.

A major limitation for the current data storage system concerns the writing speed of the bits. Currently this rate is capped at *several nanoseconds* per bit [4]. This lower limit is set forth by the random switching of the magnetic bits under influence of strong magnetic fields that change direction within these ns timescales. This indeterministic switching behaviour makes data writing impossible [5]. In an effort to circumvent this limit on writing rates, several solutions have been proposed. One of these has been *all-optical magnetization switching* [4, 6, 7].

## 1.2 Increased writing rates through all-optical switching

All-optical magnetization switching is a phenomenon occurring after certain magnetic materials absorb femtosecond laser pulses, whereby no other auxiliary magnetic fields are used to cause switching. The fact of the switching process taking place within a *picosecond* and the absence of the auxiliary fields are noteworthy as these significantly improve the writing speed of storage devices. This is due to the current data storage technology relying heavily on the conversion of *optical* data into an *electronic* signal before data can be stored as *magnetic* bits on the storage

device. Using all-optical switching removes the necessity for this opto-electric and electro-magnetic conversions thus lowering the bound on the writing speed to the order of *picoseconds*. Furthermore is expected that using this entirely optical process leads to more energy efficient magnetic storage technologies than are currently available [4].

The materials in which all-optical magnetization reversal has been detected so far are ferrimagnetic alloys containing the rare-earth metal *Gadolinium*, in particular GeFeCo. Although the switching properties of GeFeCo are excellent, the use of these alloys for *high density* data storage are limited due to (i) their lows anisotropy and (ii) amorphous structure [8]. Fortunately using *synthetic* ferrimagnetic materials is a viable possibility in order to circumvent the problems related to ferrimagnetic alloys.

In the next section a brief discussion on the physics behind all-optical switching will be presented. This discussion consists mainly of an intuitive description of the so called *RKKY coupling* which is the important interaction behind all-optical magnetization reversal in *synthetic* ferrimagnets.

## 1.3 Intuitive model of RKKY coupling

Up until now the phenomenon of magneto-optical reversal is only found to occur in ferrimagnetic alloys containing the rare-earth metal Gd. However, as mentioned previously, Gd is unsuitable for high density data storage thus making synthetic ferrimagnets interesting. As will be discussed in the next chapter the structure that should enable all-optical switching in these synthetic materials consists of a stack of ferromagnetic layers with a non-magnetic spacer layer in between. These ferromagnetic layers mimic the *sublattices* in a ferrimagnetic alloy while the spacer layer accommodates the *antiferromagnetic interaction* between the layers. However, it is important to keep in mind that the antiferromagnetic interaction in ferrimagnetic alloys is brought forth by the direct exchange interaction (see Chapter 2) while in synthetic ferrimagnets the so called *RKKY interaction* is the cause. The theory of this interaction was developed in the 1950s by Ruderman, Kittel, Kasuya, and Yosida [9, 10, 11] and describes the interaction between magnetic layers separated by a non-magnetic spacer layers. In order to understand the process behind all-optical switching in synthetic ferrimagnets it is essential to understand the RKKY interaction.

For simplicity, the potential landscape of a synthetic magnetic is modelled one-dimensionally with constant, although dissimilar values, for the magnetic layers and the non-magnetic spacer layer in between. In Figure 1.1 one of these interfaces is depicted.

If a free conduction electron in the spacer layer is considered to be travelling to the right, it will encounter a step in the potential energy due to a discrepancy between the band structures of the magnetic and non-magnetic material. This step causes the quantum mechanical wave function of the electron to be partially transmitted to the magnetic layer as well partially reflected back into the spacer layer. This reflection of the wave function gives rise to a standing wave within the well formed by the potential steps of the magnetic layers.

The RKKY theory is further elaborated by taking into account the *intrinsic spin* of the electrons. The reason for this is a height difference in the potential step an electron experiences depending on whether its spin is aligned parallel or anti-parallel with the majority of spins in the material through which it is partially transmitted. In the case of *parallel* aligned spins the potential step is *lower* than in the case of anti-parallel aligned spins. A consequence of this difference in the step potentials is the amplitude of the standing waves being dependent on the spin. The two now different standing waves interfere with each other forming a spin density wave. Integration of the spin density wave over the electron energies not larger than the *Fermi energy* results in the *total spin density*.

The oscillatory behaviour of the spin density as function of the thickness of the non-magnetic

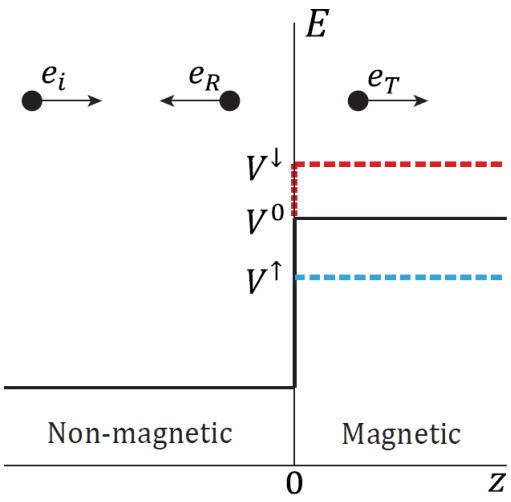


**Figure 1.1:** *Schematic representation of an incoming free conduction electron that is either transmitted past or reflected off the NM/FM interface. The potential step the incoming conduction electron experiences depends on its intrinsic spin. Retrieved from [12]*

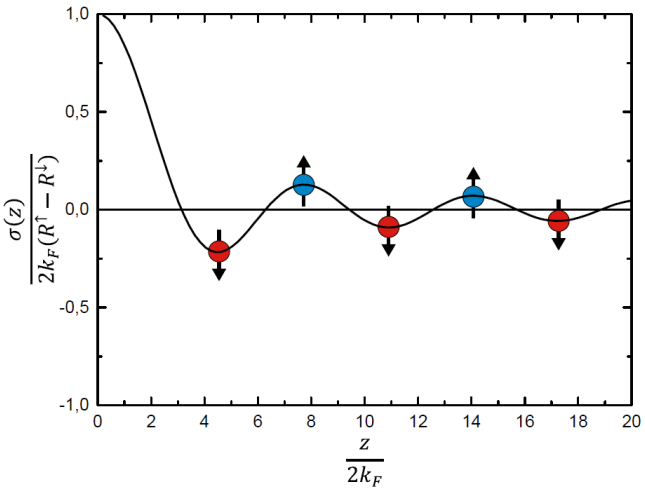


**Figure 1.2:** *The total spin density as a function of the spacer layer thickness. The arrows indicate whether the layers will be coupled antiferromagnetically (down) or ferromagnetically (up) for the corresponding spacer layer thicknesses. Retrieved from [12].*

spacer layer can be seen in Figure 1.2. The up- and downward directed arrows indicate how the different ferromagnetic layers on both sides of the space layer would have been coupled for a certain spacer layer thickness. If the spacer layer has a thickness for which the total spin density wave is *positive* the magnetic layers are said to be coupled *ferromagnetically*. In this case the magnetization of the different magnetic layers are aligned parallel with respect to each other and the material is *ferromagnetic*. On the other hand, if the thickness of the spacer layer is such that the spin density wave is *negative* the layers are *antiferromagnetically* coupled. This implies that the magnetization of the two magnetic layers are aligned anti-parallel and, depending on the magnitude of the magnetization within a layer, are characterized as being *antiferromagnetic* or *ferrimagnetic*. By choosing an adequate spacer lacer thickness a synthetic ferrimagnet can thus be constructed that is suitable for all-optical magnetic switching.

In the upcoming two sections a general description of the project will be given as well an outline of this thesis.

## 1.4 Project description

The ultimate goal of this project is *achieving single pulse all-optical switching in synthetic ferrimagnets*. This ferrimagnet will be constructed by integrating into one sample different ferromagnetic layers which are separated by a non-magnetic spacer layer. Before being integrated into one sample, the magnetic characteristics of the materials have to be scrutinized as these have to meet certain requirements, which are discussed in depth later on. These requirements are (i) a significant difference in demagnetization time for each ferromagnetic layer and (ii) the antiferromagnetic coupling of these two layers. Keeping in mind that gadolinium is not suitable for high density data storage, the use of it will be avoided.

The focus of the project as presented in the upcoming chapters is to determine the demagnetization times of several ferromagnetic thin films and subsequently determine what pair of samples could potentially be integrated within a synthetic ferrimagnet as to enable all-optical magnetic reversal. More specifically, several thin film samples will first be grown by sputtering process and then examined with a static MOKE setup to control whether their magnetization is directed out-of-plane. If this is the case, thereupon, time-resolved MOKE is used to determine the demagnetization times of the samples. From these measurements conclusions can be drawn concerning the suitability of each sample within an antiferromagnetically coupled stack.

## 1.5 Thesis outline

In this thesis the following will be discussed. In **Chapter 2** the physics concerning magnetostatics will be formally introduced followed by a section devoted to the phenomenon of all-optical switching with an historical overview of research done on the subject and a qualitative description of the mechanism behind opto-magnetic reversal. In **Chapter 3** both the fabrication technique, i.e. sputter deposition, as well as the characterization techniques used to investigate the samples are introduced, namely the earlier mentioned static and time-resolved MOKE, respectively. In these sections light is shed on the working principles of these fabrication and characterization techniques. The succeeding **Chapter 4** starts with a presentation of the strategy used for the analysis of the data gathered during the different experiments as well as the experimental results themselves. These results will be accompanied by a discussion which will form the basis of the conclusions in **Chapter 5**. In this last chapter the thesis will conclude with the contemplation of the possibilities for future experiments.

# Chapter 2

# Theory

*In this chapter the basic theory of magnetism, in particular magnetostatics, is introduced in order to be better equipped to interpret the experimental results. First the different kinds of magnetism are explored. Thereafter the magnetic energy associated with magnetic bodies is discussed as well as the phenomenon of magnetic hysteresis. This chapter continues with a section on the phenomenon of all-optical switching which, more specifically, commences with a historical overview of research done on this topic and is followed by an explanation concerning the origin of all-optical switching in synthetic ferrimagnets.*

## 2.1 Magnetostatics

### 2.1.1 Different forms of magnetism

Magnetic behaviour is generally caused by the presence of unpaired electrons in the outer shells of individual atoms or ions within the material. Besides these unpaired electrons, another important factor influencing the magnetic behaviour is temperature. The different kinds of magnetic behaviour are classified into five categories and are characterized as being (i) diamagnetic, (ii) paramagnetic, (iii) ferromagnetic, (iv) antiferromagnetic, or (v) ferrimagnetic.

The categories of magnetism are illustrated in Figure 2.1 in which diamagnetism is disregarded. This is due to the fact that all materials are inherently diamagnetic and thus only those materials which do not have stronger magnetic effects present are labelled as diamagnetic. *Diamagnetic* materials are furthermore characterized by their completely filled or empty atomic or molecular orbits. This shell configuration ensures the absence of unpaired electrons causing, therefore, the net magnetic moments of the material to be zero. When a diamagnet is influenced by an external field the magnetic flux in the atoms changes. *Lenz's law* dictates that as a response of this change in flux, a current, thus magnetic field, will be generated that opposes the external field. This diamagnetic effects persist as long as the presence of the external field.

*Paramagnetic* properties are caused by magnetic moments in the material of which the coupling is weak enough to be disturbed by thermal fluctuations. In the absence of an external field the magnetic moments are thus characterized by all being randomly orientated, resulting in a net magnetization of zero. However in case an external field is applied a paramagnet responds through the alignment of a small fraction of the magnetic moments with the field direction. As a consequence the magnetic flux inside the material is fractionally increased.

*Ferromagnetism* is caused by the accumulative effect of unpaired electrons in the outer shells of the individual atoms or ions in the material. These unpaired electrons give rise to magnetic moments that are equal in magnitude and aligned parallel to each other such that a spontaneous

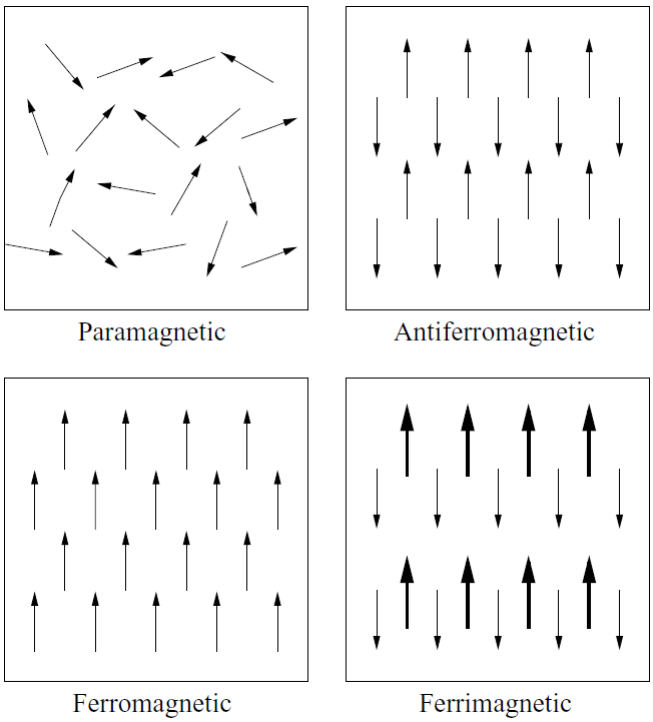


**Figure 2.1:** *The alignment of magnetic moments within magnetic materials in case of paramagnetism, aniferromagnetism, ferromagnetism, and ferrimagnetism. Retrieved from [1].*

magnetization is present. The order in the magnetic moments is a consequence of the *direct exchange interaction* between spins in the material while the *Zeeman effect* causes the magnetization to align to an external field. As a result the magnetic flux inside a ferromagnetic is higher than outside the material in the presence of an external field. Both the exchange interaction as well as the Zeeman effect will be elaborated in the next subsection.

In the context of ferromagnets the magnetization is maximized at zero temperature but diminishes for an increasing temperature. This demagnetization continues until a critical temperature, i.e. the *Curie temperature*, is reached at which the ferromagnetic properties of the material are lost. At the Curie temperature the common direction to which all magnetic moments previously aligned, is replaced by a random alignment for each magnetic moment due to thermal fluctuations. At this stage ferromagnetism has thus been replaced by *paramagnetism*.

*Antiferromagnets* resemble ferromagnets insofar they have unpaired electrons generating magnetic moments. However, for antiferromagnetic behaviour to be present, two different sublattices containing these magnetic moments need to be coupled antiferromagnetically. This implies that spins in one sublattice are aligned anti-parallel to spins in another. As the amount of spins in each direction is equal as well as the magnitude of the magnetic moments, this results in a net magnetization of zero. In the presence of an external field the reaction of antiferromagnetic materials matches that of paramagnetic materials. Analogous to the Curie temperature for ferromagnets there is the *Néel temperature* for antiferromagnets. At this temperature antiferromagnetic properties are lost as thermal fluctuations will disturb the order of the magnetic moments in the material again enabling *paramagnetic* behaviour.

*Ferrimagnets* are similar to antiferromagnets concerning the anti-parallel orientation of the magnetic moments in two different sublattices of the material. However, a difference in magnitude

of these coupled sublattices is what characterizes ferrimagnets and gives rise to a non-zero net magnetization. As in the case of ferromagnetism, the magnetic flux, under influence of an external field, is higher inside than outside ferrimagnetic material.

As the two sublattices of ferrimagnets are directed anti-parallel a temperature increase will first cause each sublattice to demagnetize up to the point that both sublattices are equal in magnitude, though non-zero, hence causing the ferrimagnet to have net magnetization of zero. The temperature at which this occurs is the *compensation temperature*. If the temperature increases even further another critical temperature is reached at which both the sublattices have a zero magnetization. At this point, as for ferro- and antiferromagnets, paramagnetic behaviour is displayed and the spontaneous magnetization of the ferrimagnet disappears.

This section continues with a discussion on different sources responsible for contribution to the total magnetic energy of a magnetic body.

### 2.1.2 Magnetic energy

The total magnetic energy $U$ associated with a magnetic body is a summation of several distinct energy contributions. In the context of the experiments described in this thesis the relevant contributions are (i) the exchange energy, (ii) the Zeeman energy, (iii) the anisotropic energy, and (iv) the demagnetization energy. Minimalizing the total magnetic energy of a magnetic body gives the *static equilibrium spin configuration* of that body. In other words, how the spins (i.e the magnetization $\mathbf{M}$) within the volume are aligned under influence of one or more of the four effects as to minimize the total magnetic energy. Each effect or contribution to the total energy, is represented as a term in the following expression for $U$ [13]:

$$U = \int_V \left[ \frac{A}{|\mathbf{M}|^2} (\nabla \cdot \mathbf{M})^2 - \mu_0 \mathbf{M} \cdot \mathbf{H}_{\text{ext}} + K_{\text{eff}} \cos^2 \theta \right] \mathrm{d}V. \tag{2.1}$$

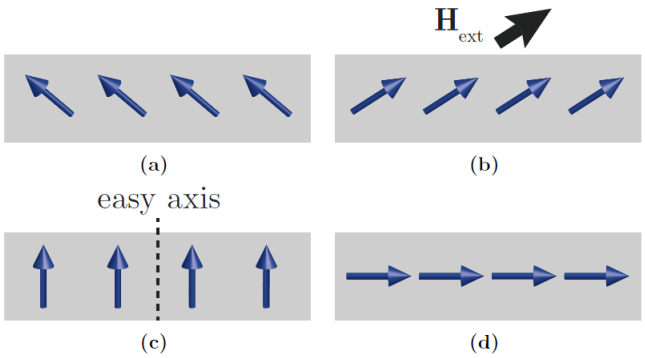


**Figure 2.2:** *Various energy contributions to the total magnetization energy of a magnetic volume ultimately determining its preferential magnetization direction. The contributions originate from* **(a)** *the exchange interaction,* **(b)** *the Zeeman effect,* **(c)** *the magnetic anisotropy, and* **(d)** *demagnetization. Retrieved from [14].*

The first term (Figure 2.2a), the *exchange energy*, is proportional to the the exchange stiffness $A$, which is a measure of the strength of the interaction, and proportional to the divergence of the magnetization $\nabla \cdot \mathbf{M}$. Minimization of this exchange term requires that the spins are aligned parallel with respect to each other. Due to the isotropic nature of the exchange interaction, the spins have no preference concerning the direction of alignment.

The *Zeeman energy* is represented by the second term (Figure 2.2b) and concerns the energy contribution as a results of an external magnetic field $\mu_0 \mathbf{H}_{\text{ext}}$ being applied to the magnetic material. The magnetic permeability in vacuum is given by $\mu_0$. Through parallel alignment of the magnetization with the external magnetic field the dot product within the Zeeman energy term is minimized.

The third energy term concerns the magnetic anisotropy which is the preference of the magnetization for a certain direction even in the absence of an applied field. That particular direction is called the *easy axis*. The magnetic energy takes this anisotropic effect into account by means of the *effective anisotropy constant* $K_{\text{eff}}$. This effective anisotropic energy is brought forth by two contributions caused by (i) the *magneto-crystalline anisotropy* (MCA, Figure 2.2c) and (ii) the *demagnetization energy* (Figure 2.2d). The effective anisotropy energy term can be decomposed into

$$K_{\text{eff}} \cos^2 \theta = K_u \cos^2 \theta - \frac{\mu_0}{2} \mathbf{H_D} \cdot \mathbf{M}. \tag{2.2}$$

The first term depends on both the demagnetization energy as well as the MCA while the second only depends on the demagnetization energy.

The origin of the MCA can be understood intuitively through a semi-classical model by considering an electron rotating around a nucleus. If the rest frame is attached to the nucleus, the electron will not experience a magnetic field. However, if the rest frame is attached to the electron instead, the positively charged nucleus seems to rotate around it, generating a magnetic field in the process. This field interacts with the spin, the intrinsic magnetic moment of the electron, hence establishing *spin-orbit coupling*. Since the crystal lattice is able to incur anisotropy in the electron's orbital moment, the electron's spin and therefore the magnetization direction is affected as a results of this spin-orbit coupling.

The demagnetization energy is the factor behind the last term in equation 2.2. Minimizing this energy implies the minimization of stray fields which are generated by the uncompensated magnetic moments at the surface of the material. These magnetic moments at the surface give rise to the demagnetization field $\mathbf{H_D}$ directed anti-parallel to the magnetization. For thin films the stray fields are minimized, i.e. the demagnetization energy is minimized, with the preferred magnetization direction along the longest axis of the magnetic volume, as in this case the surface with uncompensated moments is the smallest.

The first term in equation 2.2 can be decomposed even further by realising that atoms in the bulk have a distinct crystalline environment compared to atoms at the surface. As a results it can be made reasonable that the anisotropy constant $K_u$ can be expressed as a function of the *volume* and the *surface anisotropy constants*, respectively $K_v$ and $K_s$ [15], as

$$K_u = K_v + \frac{2K_s}{t}. \tag{2.3}$$

The thickness of the magnetic layer is given by $t$. The factor 2 is necessary for it takes into account the contribution from the top and bottom surface. The first term in this equation, i.e. the volume anisotropy, is dominated by the demagnetization energy, while in the surface anisotropy the MCA is the only factor playing a role. In the case of thin ferromagnetic films ($t \sim 1\,\text{nm}$), which are used in this project, the surface term in equation 2.3 dominates. As surface anisotropy prefers an *out-of-plane* magnetization, this explains the occurrence of *perpendicular magnetic anisotropy* (PMA) in the ferromagnetic samples. How this PMA in samples changes under influence of an external field applied parallel to it is discussed next.

### 2.1.3 Hysteresis

In general terms *hysteresis* is the phenomenon of the current state of a system being dependent on its past state. Magnetic hysteresis occurs when an external field is applied to ferro- or ferrimagnetic materials upon which their magnetic moments align to this field. In the case of ferromagnetic thin films with PMA, which are used in the experiments, above a certain out-of-plane field strength the magnetization switches abruptly from a minimum to a maximum value. This magnetization maximum is called the *saturation magnetization* $M_S$ while the applied field at which this switch takes place is the *coercive field* $H_C$ (see Figure 2.3). If now the field strength is weakened to a positive value below that of the coercive field, the magnetization of the material remains, even for $H = 0$. Negative values for the external field imply a reversal in direction which results, due to the symmetry of the system, in a magnetization switching from its maximum to its minimum of $-M_S$ for a field of $-H_C$.

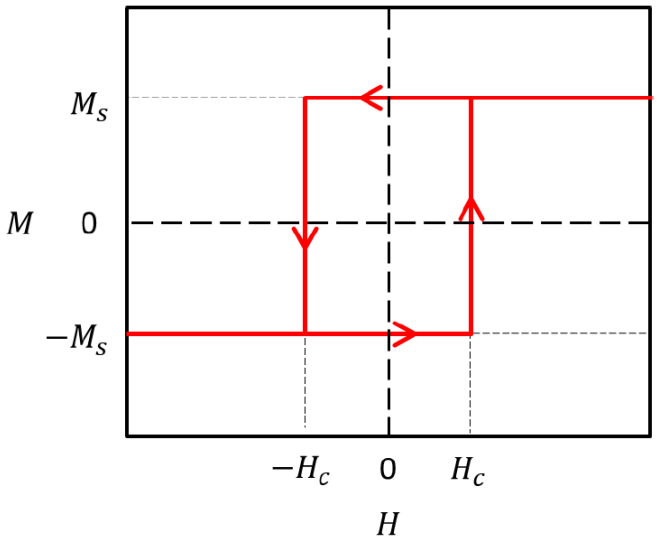


**Figure 2.3:** *This hysteresis loop shows the magnetization as function of the external field strength directed along the easy axis as obtained through the Stoner-Wohlfart model for magnetic thin films. Retrieved from [16].*

The hysteresis loop as depicted in Figure 2.3 shows the magnetization direction of the material for a varying applied field parallel to the easy axis. The particular form of the loop can be obtained through the *Stoner-Wohlfarth model* [17]. In the Stoner-Wohlfarth model, assuming a zero temperature and an ideal homogeneous sample, only the Zeeman energy (second term) and anisotropic energy (third term) in equation 2.1 are considered. The magnetic energy density $u$ is hence given by

$$u = -\mu_0 M H_{\text{ext}} \cos\theta + K_{\text{eff}} \cos^2\theta, \tag{2.4}$$

with $\theta$ the angle between the easy axis and the magnetization direction. Minimization of this expression gives the earlier mentioned magnetization as function of the applied field, i.e. the squared hysteresis loop. The coercive field, furthermore, can be related to the saturation magnetization through

$$H_C = \frac{2K_u}{\mu_0 M_S}. \tag{2.5}$$

Non-zero temperatures and imperfections of samples affect relevant parameters of the Stoner-Wohlfarth hysteresis loop. At non-zero temperature the anisotropic energy barrier can be surmounted by thermal fluctuation, causing magnetization switching, before an external field has reached $H_C$. Hence, the strength of the applied field at which the material switches magnetization is lowered.

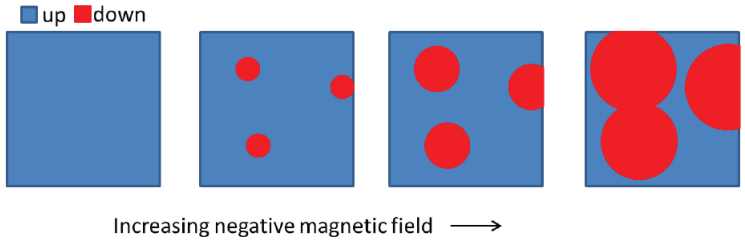


**Figure 2.4:** *An initially upward saturated thin film under influence of an increasingly downward external field. Domains of opposite magnetization nucleate and increase in size untill the whole sample has undergone magnetic reversal. Retrieved from [16].*

Examples of imperfections in samples are contaminations, thickness variations and (blunted) edges. These factors cause local variations in the anisotropy of a sample as a result of which certain regions of the sample switch magnetization before others. This process of magnetization switching in regions of lower anisotropy is called *nucleation*. After domains opposite magnetization have nucleated, the domain wall, i.e. the narrow region where opposite magnetization directions transition into each other, can propagate further until the whole sample has switched magnetization. Magnetic reversal of a sample through nucleation is shown in Figure 2.4.

Keeping in mind the ultimate goal of this project and having reviewed relevant magnetostatic concepts, the next section will focus on all-optical switching.

## 2.2 All-optical switching

### 2.2.1 Historical overview

Research on the effect of femtosecond laser pulses on the magnetization of metallic materials on picosecond timescales began in 1996 when Beaurepaire *et al.* reported that ferromagnetic nickel, upon absorption of fs pulses, reponds by a reduction of the magnetization of the material [6]. This was surprising as earlier experiments done on Ni with picosecond pulses had shown no sign of demagnetization up to its melting point [18]. As can be seen in Fig 2.5 the demagnetization process is characterized by a rapid drop in magnetization, taking place within a picosecond, after which, over significantly larger timescales, the magnetization returns to its original value.

In an attempt to describe the above described demagnetization, Beaurepaire *et al.* developed a phenomenological model, the *3 Temperature Model* (3TM). This model is an extension of the *2 Temperature Model* (2TM) which describes, by means of two coupled differential equations, the electron and phonon dynamics after pulsed laser excitation. In these 2TM equations the energy transfer between electrons and phonons is incorporated. However, if now the phonon and electron systems are allowed to interact with a third system, namely a spin system, the earlier mentioned 3TM is constructed. Although the addition of the spin system was made solely on a phenomenological argument, the demagnetization dynamics as obtained theoretically through the 3TM satisfactorily described the experimental results [19].

Although the demagnetization of ferromagnetic Ni was thus reported to occur after the absorption of fs laser pulses, no magnetization reversal was observed. Magnetic reversal caused by pulse absorption was not reported until a decade later.

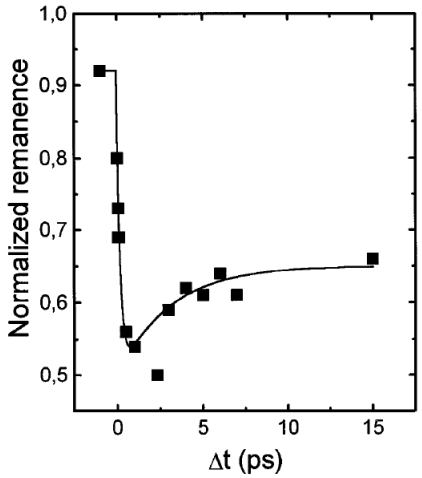


**Figure 2.5:** *Rapid demagnetization of ferromagnetic Ni after absorption of fs laser pulses. Retrieved from [6].*

Actual magnetization switching, specifically single-shot switching, was first presented by Stanciu *et al.* [7]. In their experiments the ferrimagnetic GdFeCo alloy was used to absorb fs laser pulses while no magnetic field was applied. What the group found was that the magnetization of the film would reverse deterministically depending on the *helicity* of the absorbed laser pulse while *linearly* polarized light did not cause magnetic switching. The helicity dependent switching is shown in Fig 2.6. The domain with magnetization initially directed *downwards* (dark region) is consequently being switched by only *right* circularly polarized light while leaving the domain with upward magnetization (light region) untouched. The opposite happens for initially *upwards* directed magnetization. Now these region are left untouched by *right* circularly polarized light, while experiencing reversal for *left* circularly polarized light. An important application of the discovery of the above described phenomenon was immediately recognized, namely as *'(...) an ultrafast and efficient pathway for writing magnetic bits at record-breaking speeds'* [7].

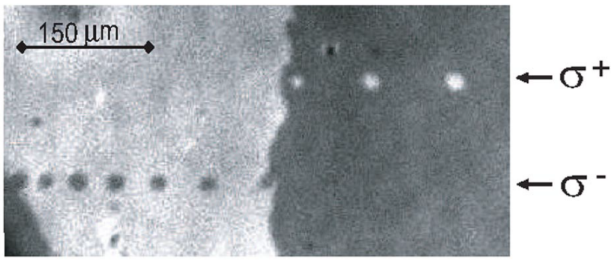


**Figure 2.6:** *Single-shot all-optical switching of thin film GdFeCo by right ($\sigma^+$) and left ($\sigma^-$) circularly polarized light. Retrieved from [7].*

All-optical switching in synthetic ferrimagnets came closer with the findings of Ostler *et al.*

in 2012. Not only did they show experimentally that, without using a magnetic field, all-optical magnetic reversal was possible in thin film GdFeCo with *linearly* polarized light but they also replicated their experimental findings numerically by assuming that the switching mechanism was driven by rapid heating of the medium after absorption of a fs pulse [4]. In order words, the group found that heating alone is sufficient to cause deterministic magnetization reversal. This conclusion led to an explanation of the previously mentioned helicity-dependent switching. This switching behaviour was thus a consequence of using a laser with an intensity below a certain threshold and of the material's circular dichroism.

An important result of the experimental work done by Ostler *et al.* is presented in Fig 2.7. Here can be seen how a single fs pulse of linearly polarized light consequently switches the magnetization of the domains, ignoring the initial direction of magnetization. Thus every second pulse ($N$ even) absorbed by the sample results in a magnetization pointing in the same direction as before absorbing any pulse at all, i.e. for $N = 0$.

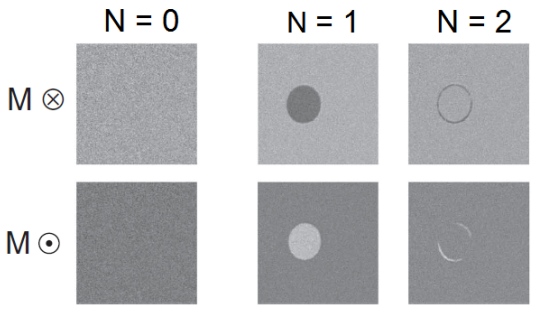


**Figure 2.7:** *Single-shot all-optical switching in thin film GdFeCo achieved through the absorption of linearly polarized laser pulses. Retrieved from [4].*

In Fig 2.8a numerical results are presented showing the change in magnetization for individual sublattices of GdFeCo due to absorbed laser pulses. The Fe sublattice has a demagnetization time smaller than that of the Gd sublattice thus, when the Fe sublattice has been demagnetized completely, the non-zero magnetization of the Gd sublattice (see Figure 2.8b) gives rise to a transient ferromagnetic state of the material. Thereafter, the magnetization of the Fe sublattice changes direction due to the antiferromagnetic exchange interaction between the sublattices before relaxing to the switched state. This reversal happens after every laser pulse.

Experimental confirmation that the magnetization of GdFeCo after laser pulse absorption behaved as the simulations predicted (see Figure 2.8), was presented by Radu *et al.* in [20]. In their experiments the group used the so called *X-ray magnetic circular dichroism* (XMCD) technique which enabled them to determine the magnetization direction of the individual sublattices. The results of the time-resolved measurements are shown in Figure 2.9. Here can be seen how, as in the simulations, each of the Ge and Fe sublattices demagnetize after absorption of a fs pulse thus giving rise to a transient ferromagnetic state.

It is clear from the above mentioned articles that single-shot all-optical switching is possible in ferrimagnets. Unfortunately, these alloys contained the rare-earth metal Gd and are, as mentioned in section 1.1, not suitable for fast data storage, which explained the requirement of synthetic multilayer composition without Gd. However, up until now, no reasons have been given why *synthetic* ferrimagnets are expected to show similar behaviour as as GdFeCo to the absorption of fs pulses and therefore be suitable for all-optical switching.

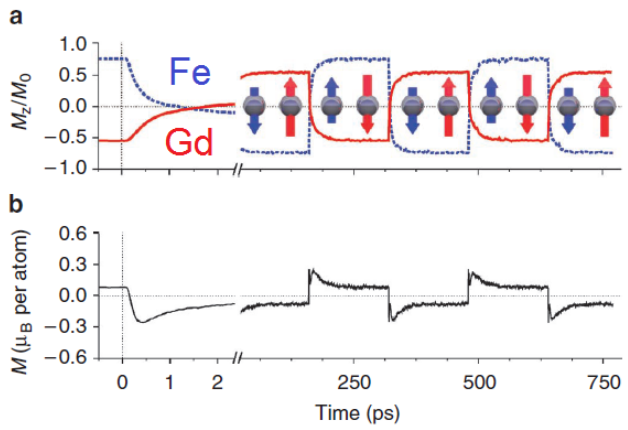


**Figure 2.8:** **(a)** *Simulation of the demagnetization process in the Gd and Fe sublattices.* **(b)** *Differences in demagnetization times give rise to a net magnetization of the material. Retrieved from [4].*

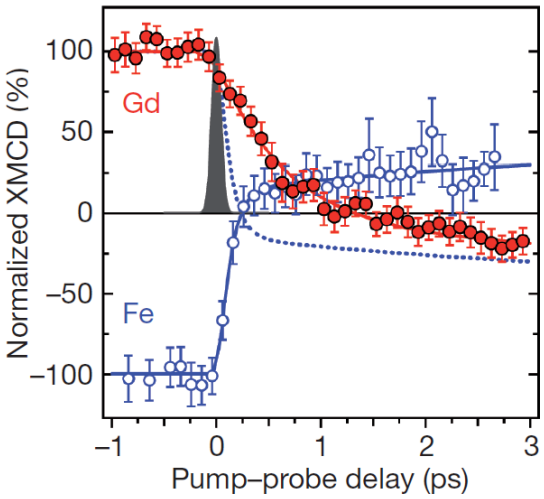


**Figure 2.9:** *Time-resolved measurements of Fe and Gd magnetic moments after pulse absorption as obtained through XMCD. The Fe sublattice clearly demagnetizes and switches before the Gd sublattice. The solid gaussian profile indicates the experimental time resolution while the dashed blue line is the Fe magnetization mirrored in the horizontal axis.*

### 2.2.2 All-optical switching in synthetic ferrimagnets

As mentioned before, all-optical magnetization reversal in ferrimagnetic *alloys* is caused by heating alone. A phenomenological description of this process will first be given, before focusing on this switching process in *synthetic* ferrimagnets.

In ferrimagnetic alloys, for example GdFeCo, this process is initiated after a laser pulse rapidly increases the thermal energy of the electronic system of the material causing fast energy transfer into the spin system. The thermal energy is high enough for the spins to experience temperatures higher than the Curie temperature leading to demagnetization. Differences in magnetic moment between the Gd and Fe sublattices let the demagnetization process take place on different timescales. The Fe sublattice reaches zero magnetization before the Gd sublattice causing a transient ferromagnetic state of the material due to a brief parallel alignment of the magnetic moments. While the Fe sublattice has already switched, the Gd sublattice still lags behind. It is the antiferromagnetic exchange interaction that forces the magnetization of the Gd sublattice to reverse, finally driving the system is driven to a magnetic equilibrium. Inspired by all-optical switching in ferrimagnetic alloys, the possibility of this switching process in synthetic ferrimagnets was first investigated with simulations by Evans *et al.* [8]. The group focused on synthetic ferrimagnets, Fe/FePt bilayers in particular, that consisted of two transition metal ferromagnetic layers that were antiferromagnetically coupled by means of a non-magnetic spacer layer (see Figure 2.10). The simulations for these Fe/FePt structures confirmed that besides antiferromagnetic coupling between ferromagnetic layers also distinct demagnetization times are a requirements for enabling all-optical switching in synthetic ferrimagnets.

Material choices for the spacer layer are elements as Ir, Si, and Ru while manipulating the thickness of this layer can be used to regulate the interlayer coupling that, as discussed in 1.3, is

brought forth by the RKKY interaction. Concerning the thickness of the ferromagnetic layers a balance has to be found between two opposing effects, namely (i) the inversely proportional relation between the coupling strength and the layer thickness and (ii) the thermal stability which increases for increasing volumes. Generally, the right balance seems to be achieved by having a thicker layer made of material with high anisotropy while the other layer can be thin to optimize the coupling strength.

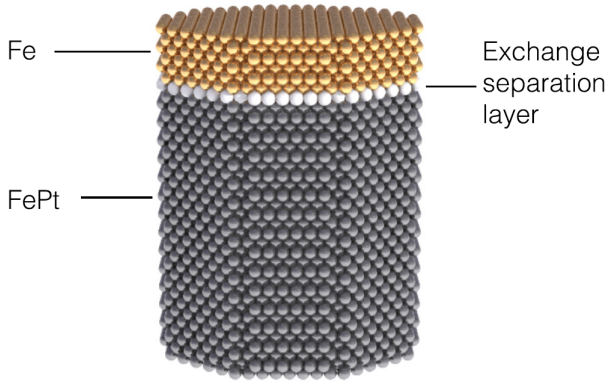


**Figure 2.10:** *Composition of the synthetic ferrimagnet Evans et al. found to be suitable for all-optical magnetization reversal. The ferrimagnet is comprised of Fe and FePt layers that are antiferromagnetically coupled by means of a non-magnetic spacer layer.*

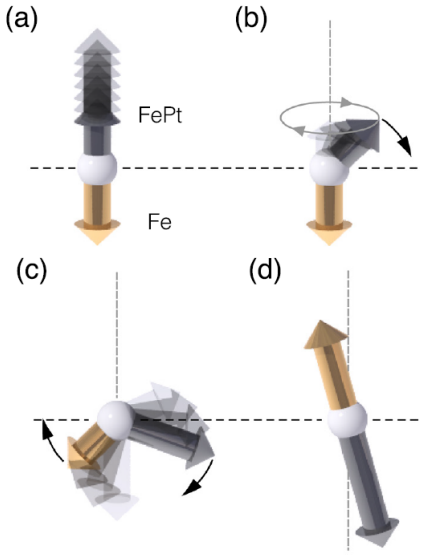


**Figure 2.11:** *The process of all-optical magnetization reversal.* **(a)** *After absorption of a fs laser pulse the FePt layer rapidly demagnetizes.* **(b)** *Thermal fluctuations lead to a transverse component of the magnetic moment of the FePt layer starting a rapid precession into the exchange field of the Fe layer.* **(c)** *The Fe layer finally starts responding to the laser pulse absorption by initiating the precession of its magnetic moment into the exchange field of the FePt layer.* **(d)** *Ultimately, on longer timescales, switching is completed after thermal equilibrium is reached by the Fe and FePt layers. Retrieved from [8].*

The process of all-optical magnetization reversal in the synthetic ferrimagnet is shown step-by-step in figure 2.11. Initially, the magnetic moments of the two ferromagnetic layers are aligned anti-parallel with respect to each other. Upon absorption of a fs laser pulse, the layer with the smallest demagnetization time, i.e. FePt, is heated above its Curie temperature subsequently demagnetizing within a picosecond. The Fe layer is still characterized by significant degree of order in the magnetic moments (Figure 2.11a). While the FePt layer is demagnetized, the thermal energy fluctuation are large enough to contribute a small, nonetheless influencing, transverse component to the magnetic moment. This leads to a rapid precession of the magnetic moment of the FePt layer into the exchange field of the Fe layer where it relaxes (Figure 2.11b). During the precession of the FePt layer the

slowly responding Fe layer starts to precess in the increasing exchange field of the FePt layer after finally perceiving the absorption of the laser pulse. Simultaneously the ferrimagnet experiences a transient ferromagnetic state (Figure 2.11c). Magnetization reversal is achieved after the Fe and FePt reach thermal equilibrium on longer timescales (Figure 2.11d).

Although all-optical switching is a thermally activated process, the mechanism behind it is characterized as being deterministic. Taking into account the importance of the exchange coupling in this process, it should not be deemed surprising that the strength of this antiferromagnetic coupling determines the timescale at which the magnetization switching occurs and the rate of angular momentum transfer between the ferromagnetic layers. Ideally this coupling should be as strong as possible to ensure fast dynamics.

## 2.3 Summary

In this chapter magnetostatic theory was introduced focusing on the different forms of magnetism as well as the magnetic energy associated with magnetic bodies and the origin of the contributions to it. Furthermore was explained why ferromagnetic thin films could have PMA, hence an out-of-plane magnetization, which is thus due to fact that in thin films the surface anisotropy, which prefers out-of-plane magnetization, dominates the volume anisotropy, which prefers in-plane magnetization. Finally was discussed in the first section how to obtain the squared shape of the easy axis hysteresis loop through the Stoner-Wohlfart model for magnetic thin films, what the characteristics are of these loops, and how the loop's shape is influenced by imperfection in the samples.

In the second section the results of several scientific papers are presented giving insight into the developments of research done on the subject of all-optical switching. This research amounted to the discovery of single-shot all-optical switching in ferrimagnetic alloys, e.g. GdFeCo, and the insight that this reversal process is completely driven by thermal forces. Another important conclusion is the fact that antiferromagnetic coupling between sublattices is necessary to enable optical magnetic reversal. Ultimately in this section, an article is presented in which simulations support the possibility of all-optical switching in synthetic ferrimagnets. This article confirmed that besides antiferromagnetic coupling between the ferromagnetic layers of the synthetic ferrimagnet also a distinct demagnetization time is necessary between the layers. Finally, the switching process is elaborated step-by-step for these synthetic structures and is discussed how to optimize the switching dynamics, which is through a strong antiferromagnetic coupling.

Before the insight gained in this chapter is used to interpret experimental results, the next chapter will describe how samples are fabricated and thereupon investigated in order to produce the experimental results.

# Chapter 3

# Fabrication and characterization techniques

*This chapter describes how the different samples are created and what techniques are used to characterize relevant magnetic properties, both static and dynamic. First sputter deposition is presented followed by a description of the static and the time-resolved MOKE setup.*

## 3.1 Sputter deposition

The ferromagnetic thin film samples used for the measurements have been made by means of a *DC sputtering process* (see Figure 3.1). During this process, which takes place in a chamber held at high vacuum ($\sim 10^{-7}$ mbar), argon gas is inserted and ionized between a cathode and an anode ring over which a high voltage is put. The electric field then accelerates the highly energized Ar ions towards the cathode, i.e. the target, which is made of the material to be deposited. Target atoms are then knocked off which ultimately land on the substrate to condensate thus forming a thin layer. This sputtering technique enables the deposition of layers with a sub-nm precision.

As the measurements done on the samples involve high energy laser pulses it is necessary for the substrate to be made of a material which enables efficient heat transportation. The substrate is therefore chosen to be made of *boron-doped silicon*, SiB. For all samples the sputtering begins with the deposition of *tantalum* as a first layer in order to improve the quality of the sample layers by providing a smoother layer on which *platinum* can be subsequently grown. The ferromagnetic composition after this first platinum layer varies from sample to sample. However, as the top layer of the samples, always platinum is chosen to prevent oxidation of the underlying layers. In Figure 3.2 a schematic representation of the above described stack is shown.

As mentioned in section 2.1 it is necessary for the magnetization of the samples used in this project to be directed out-of-plane. In order to achieve PMA in the samples the ferromagnetic films have to be thin enough. This way the volume anisotropy, which prefers in-plane magnetization, is much smaller than the surface anisotropy, which prefers the desired out-of-plane magnetization.

In the following section the two major techniques are described by means of which the static magnetic properties and the demagnetization times of the thin film samples are investigated. These techniques are based on the *magneto-optical Kerr effect*.

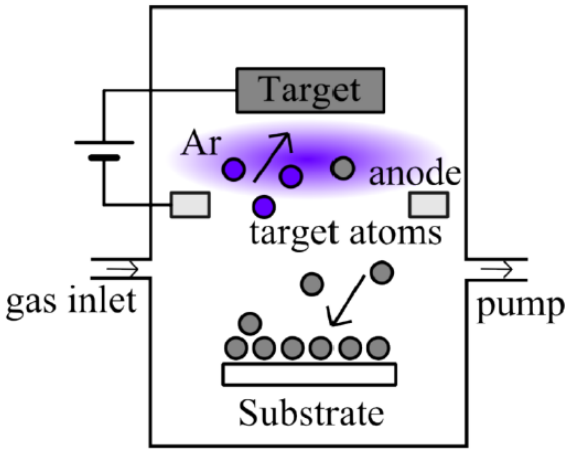


**Figure 3.1:** *Schematic representation of DC sputter deposition. Ionized argon gas is accelerated towards the target knocking off the desired material onto a substrate. Retrieved from [16].*

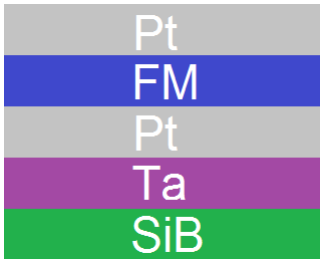


**Figure 3.2:** *Schematic representation of the sample structure used for the experiments.*

## 3.2 Characterization of magnetic behaviour

This section covers the methods used to scrutinize magnetic behaviour of the ferromagnetic samples. For these measurements both static as well as time-resolved MOKE is used. In the context of the project the static MOKE measurements serve as the primary tool by means of which ferromagnetic layers can be nominated or rejected as part of an antiferromagnetically coupled composition. Thereafter, the TR-MOKE is used to further investigate the demagnetization dynamics of the samples with out-of-plane magnetization in order to determine their demagnetization times for various laser fluences.

### 3.2.1 Static MOKE

The *magneto-optical Kerr effect* (MOKE) refers to the influence magnetic materials have on the polarization of light upon reflecting off these materials. This effect was discovered in 1877 by John Kerr [21] and works through a similar mechanism as the well-known *Faraday effect* which concerns the transmission through magnetic material. Although this mechanism is of quantum mechanical origin, the Kerr effect can be understood intuitively by realising that *linearly* polarized light can be constructed out of a linear combination of *right* and *left circularly* polarized light. As generally the velocity of light and the reflectivity of magnetic materials depend on the polarization of the incoming light, linearly polarized light will experience (i) rotation of the polarization and (ii) alteration of the ellipticity. It turns out to be that this (complex) Kerr rotation is proportional to the out-of-plane magnetization [22].

The static MOKE setup, showed schematically in Figure 3.3, is used to measure the *polar Kerr effect*, thus the out-of-plane magnetization. The setup is comprised of a laser beam being send through a *polarizer* (P1), linearly polarizing the beam at an angle $\phi_1$ with respect to the horizontal. In order to improve the signal-to-noise ratio of the signal a *photo-elastic modulator* (PEM) is placed right after P1 and used as the reference signal for a *lock-in amplifier*. The input of this lock-in amplifier is connected to the photodetector. The PEM modulates the polarization of the beam

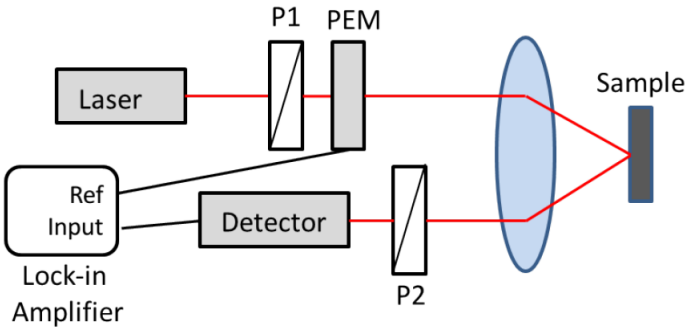


**Figure 3.3:** *Schematic representation of the static MOKE setup. The role of the various optical elements used in the setup is discussed in the text. Retrieved from [16].*

after P1 with a certain modulation frequency $\omega_{PEM}$ with as consequence that only that part of the incoming signal that is changing with the same frequency $\omega_{PEM}$ as the polarization is considered to be relevant. In other words, the lock-in amplifier filters out changes in the signal caused by polarization independent effects. After the PEM, the laser beam is reflected off the *sample* with a near zero angle of incidence, thereafter going through an *analyser* (P2). The polarization direction $\phi_2$ of P2 is set perpendicular to that of P1. This way, if the sample would not have had an out-of-plane magnetization, the polarization of the incoming beam would have only rotated 180° due to reflection off the sample, and thus would have been blocked completely by P2 and no signal could have reached the *photodetector*. If there is out-of-plane magnetization the polarization changes upon reflection and a signal reaches the detector. Now that a description of the setup has been given the *Jones matrix formalism* [23] is used to derive the signal as ultimately received by the photodetector.

The polarization of the laser beam is characterized by the vector $\mathbf{E} = (E_x, E_y)^T$. After passing through the first polarizer with transmission oriented at an angle 45° with respect to the horizontal, the Jones vector is given by

$$\begin{bmatrix} E_x \\ E_y \end{bmatrix} = \frac{1}{\sqrt{2}} \begin{bmatrix} 1 \\ 1 \end{bmatrix}. \tag{3.1}$$

This linearly polarized beam then goes through the PEM, represented by the vector

$$\mathcal{M}(t) = \begin{bmatrix} 1 & 0 \\ 0 & e^{iA\cos\omega t} \end{bmatrix}, \tag{3.2}$$

where $A$ is the amplitude of retardation between $E_x$ and $E_y$, $\omega$ the frequency of the polarization modulation, and $t$ the internal time of the PEM. The reflection off the sample is given by the matrix

$$\mathbf{S} = \sqrt{r} \begin{bmatrix} 1 & -\Theta \\ \Theta & 1 \end{bmatrix} \tag{3.3}$$

with $r$ the reflection coefficient and $\Theta$ the *complex Kerr rotation*. This complex Kerr rotation is composed of the Kerr rotation $\theta$ and Kerr ellipticity $\epsilon$ and is, as mentioned earlier, proportional to the out-of-plane magnetization $\mathbf{M} = M\tilde{z}$. Thus

$$\Theta = \theta + i\epsilon = QM \tag{3.4}$$

with $Q$ a complex constant that can be determined theoretically and experimentally [24]. Finally, the Jones matrix of the analyser is given by

$$\mathbf{P} = \sqrt{r}\begin{bmatrix} 1 & 0 \\ 0 & 0 \end{bmatrix}. \tag{3.5}$$

The signal as ultimately obtained by the detector is now given by the matrix product

$$\begin{bmatrix} E_x \\ E_y \end{bmatrix} = \frac{1}{\sqrt{2}}\mathbf{P}\,\mathbf{S}\,\mathcal{M}(t)\begin{bmatrix} 1 \\ 1 \end{bmatrix}. \tag{3.6}$$

The result of equation 3.6 can be used to determine the signal *intensity* $I$ on the photodetector through

$$I(t) = |\mathbf{E}\mathbf{E}^*| = r\left\{\frac{1}{2} + \theta\cos(A\cos(\omega\mathrm{t})) + \epsilon\sin(A\cos(\omega\mathrm{t})) + O(\theta^2, \epsilon^2)\right\}. \tag{3.7}$$

As the Kerr rotation is typically extremely small neglecting the terms of the order $\theta^2$ and $\epsilon^2$ is justified and the intensity can be approximated through *Fourier-Bessel expansion* [16]. The terms in this expansion are proportional to the harmonics $\cos(n\omega t)$ with $n \in \mathbb{Z}$. Thus

$$I(t) \approx I_0 + I_1(t) + I_2(t), \tag{3.8a}$$

wherein

$$\begin{aligned} I_0 &= r\left\{\frac{1}{2} + \theta J_0(A)\right\} = \text{constant}, \\ I_1(t) &= \epsilon r J_1(A)\cos(\omega t), \\ I_2(t) &= \theta r J_2(A)\cos(2\omega t). \end{aligned} \tag{3.8b}$$

$J_n$ represents the *n-th order Bessel function of the first kind* [25]. Equation 3.8 clarifies that both the ellipticity $\epsilon$ and rotation $\theta$ can be determined by setting a lock-in amplifier on the first or second harmonic of the PEM frequency $\omega$, respectively.

During the project *polar* MOKE setup is used to determine whether the magnetization of a certain sample is directed *out-of-plane*. More specifically, by applying a varying external field parallel to the PMA of the sample, i.e. out-of-plane, a hysteresis loop is obtained. From the shape of this loop it can be determined whether the easy-axis is directed out-of-plane. The sought-after squared shape has already been presented in Figure 2.3. However, important to keep in mind is the occurrence of an interaction between the laser beam and the applied magnetic field within the lens if it is placed close enough in front of the sample. This interaction is the earlier mentioned Faraday effect and influences the measured magnetization by causing a rotation of the polarization plane, i.e. *Faraday rotation*. The effect of Faraday rotation can easily be recognized as it adds to the squared hysteresis loop a component that increases linearly with the applied field strength. The horizontal parts of the loop are thus sloped and closed by the vertical parts. Examples of these hysteresis loops are found in Chapter 4. The coercive field strength is not altered by the Faraday effect.

### 3.2.2 Time-resolved MOKE

The second measurement tool used in the project that will be discussed is the *time-resolved MOKE* (TR-MOKE). The TR-MOKE is used to investigate the dynamic magnetization properties of the samples. The idea behind TR-MOKE is to excite a sample with a high intensity *pump* pulse upon which a low intensity *probe* pulse is used to measure the magnetization analogously to the static MOKE setup (see Figure 3.3). The *time delay* between the two pulses is varied as to determine the magnetization of the sample as a function of time. This time delay can be transformed into a *path difference* between the pump and probe beams by dividing through the speed of light. The corresponding resolution in the time domain is thus given by combining the accuracy of path difference, which is of the order $10^{-2}$ mm, and a speed of light of $3 \cdot 10^8$ m/s. Using these figures results in a time domain resolution of several *tens of femtoseconds*. This resolution for the time delay is sufficiently small to be able to investigate the rapid demagnetization in the samples after absorption of a fs laser pulse. Next, the TR-MOKE setup will be discussed in more detail.

Initially a beam splitter causes a laser pulse to be split, with a certain intensity ratio, into a *pump* and *probe* beam. These are represented by the thick and thin red lines, respectively, in Figure 3.4.

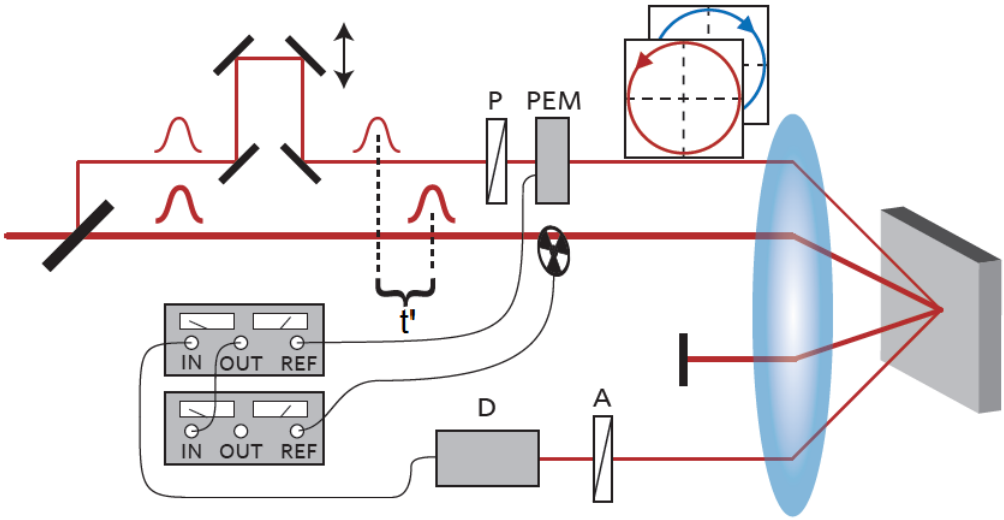


**Figure 3.4:** *Schematic representation of the TR-MOKE setup. Details of the setup are elaborated in the text. Retrieved from [19].*

First the role of the probe beam is considered before continuing with the pump probe. As mentioned earlier the probe beam within the TR-MOKE setup is used to measure the magnetization of a sample the same way as is done through static MOKE and consequently passes through the same optical elements as in the MOKE setup. First the probe is polarized linearly by a polariser (P) after which a PEM modulates the polarization with a certain frequency. After being focused on and reflecting off the sample the beam goes through an analyser (A) and ultimately reaches the photodetector (D). Now the pump beam will be examined.

After the beam beam passes the beam splitter the pump beam is modulated by means of a mechanical *chopper* which is turning at a certain frequency. Thereafter, the pump is reflected by a *retro-reflector* mounted on a *translation stage* by means of which the earlier mentioned time delay ($t'$) between the pump and the probe beam can be manipulated. Finally, the pump is focused on

and reflected off the sample before being blocked.

In order to increase the signal-to-noise ratio of the signal caused by the demagnetization process a *double modulation* technique is used. This double modulation is achieved by means of two connected lock-in amplifiers instead of one, as was the case in the MOKE setup. So, to be more specific, the first lock-in amplifier is set to the PEM frequency of which the output signal serves as the input signal of the second lock-in amplifier. The reference of this second lock-in amplifier is connected to the chopper. Ultimately this double modulation results in only pump-induced changes to be measured in the signal by filtering out optical noise in both the path of the pump and the probe hence increasing the signal-to-noise ratio.

The sample is placed inside an electromagnet coil such that the magnetic field is aligned parallel to the normal of the sample. This configuration is necessary in order to impose the desired magnetization direction of the sample after demagnetization has occurred as a results of laser pulse absorption. Two separate TR-MOKE measurement series are performed, one with the bias field directed upward, the other with the field directed downward. The results from these two measurement series are then averaged in order to eliminate the effects of the bias fields on the signal, thus yielding the Kerr rotation [22].

Focusing the pump and probe beams on the sample and determining their respective spot sizes is done by means of the *knife-edge method*. This method is elaborated on in Appendix A.

In the next chapter is described in detail how the MOKE and TR-MOKE measurements have been performed and how the data has been analysed as to obtain the final results.

# Chapter 4

# Results and discussion

*In this chapter it is described in detail how the experimental data has been obtained. First an overview will be given concerning the different ferromagnetic thin films that were fabricated by means of sputter deposition. Thereafter the results of the static MOKE measurements will be discussed followed by those of the TR-MOKE measurements. The results are accompanied by a discussion.*

## 4.1 Samples grown by DC sputter deposition

A total of four different ferromagnetic thin film samples have been grown by means of the DC sputtering process as described in section 3.1. The general composition of these four samples was given earlier in Figure 3.2. The thickness of the Ta and Pt layers are 4.0 nm and constant for all samples. The material used for the ferromagnetic part, with the layer thickness given in nanometres, are the following:

(I) $Co_{0.4}$

(II) $Co_{0.3}/Ni_{0.6}/Co_{0.3}$

(III) $Co_{0.3}/Fe_{0.6}/Co_{0.3}$

(IV) $Co_{0.3}/Fe_{0.2}/Co_{0.3}$

From now on these ferromagnetic thin films will be referred to as the **Co**, **Co/Ni**, **Co/Fe**$_{0.6}$, and **Co/Fe**$_{0.2}$ sample, respectively.

The reason for using these particular samples is the fact that these materials have been used in experiments that showed the desired magnetic switching behaviour. Yet, gadolinium was used in all ferrimagnetic structures.

Concerning the reliability of the different layer thickness of the samples an important remark has to be made. In particular the **Co/Ni** sample encountered problems during the deposition process which have significantly influenced the ultimate thickness of the Ta and Pt layers. As, on the contrary, the magnetic layers were properly sputtered the experimental results will still be regarded as significant for the project.

## 4.2 Static MOKE measurements

As mentioned before the static MOKE measurements are performed in order to determine whether the magnetization of the thin film samples is directed out-of-plane. If this is the case for a particular sample time-resolved measurements will be made thereafter.

Squared hysteresis loops were obtained for the **Co**, **Co/Ni**, and **Co/Fe**$_{0.2}$ samples using the polar MOKE setup demonstrated in Figure 3.3. A squared hysteresis loop for the **Co/Fe**$_{0.6}$ sample, on the other hand, could only be measured after significantly tilting the sample with respect to the angle of incidence of the laser. This signifies that the easy axis of the sample is not directed out-of-plane. The results of the **Co** and the **Co/Fe**$_{0.6}$ samples are presented in Figure 4.1 and 4.2, respectively, while the remaining results are placed in Appendix B. The fit through the data points is obtained by splitting the data points in two groups, namely those measured in a forward field sweep and the other in a backward field sweep. Thereafter each data set is separately fitted by a linear combination of a linear and error function fit of the form

$$y = A + Bx + C\,\mathrm{erf}\left\{\frac{x - D}{E}\right\}, \tag{4.1}$$

in which $A$ to $E$ are fitting constants. The coercive field value corresponds to the fitting constant $D$ and indicates that particular magnetic field value for which the MOKE signal is halfway between plus and minus the saturation magnetization. The fitting process is applied to both steps in the hysteresis loop, i.e. for the forward and backward field sweep, of which the results are shown in black in the respective figures.

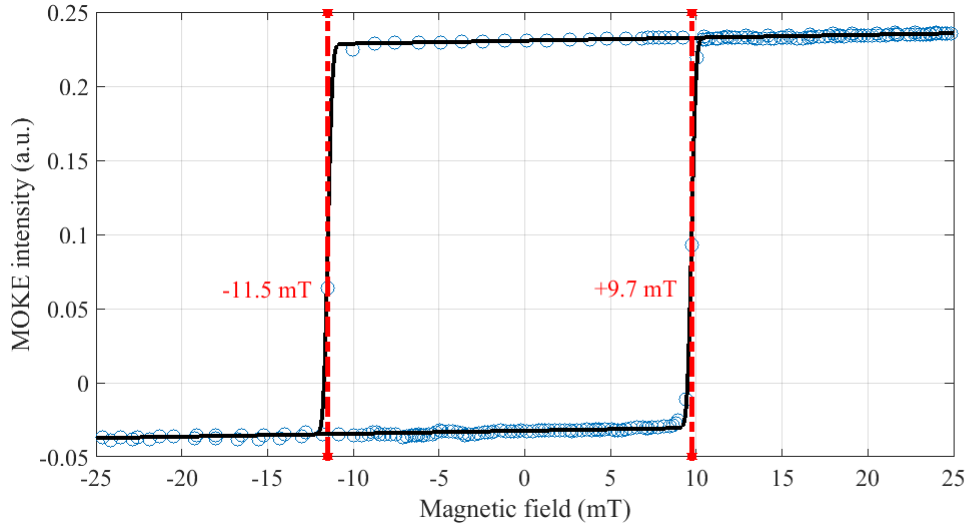


**Figure 4.1:** *The hysteresis loop of the* ***Co*** *sample as measured by means of polar MOKE. The squared shape of the loop indicates that the magnetization of the sample is directed out-of-plane. The red dashed lines give the coercive field values. The data is fitted with equation 4.1.*

The sensitivity to the polar MOKE measurements revealed whether the magnetization of the samples were or were not directed out-of-plane. For the **Co**, **Co/Ni**, and the **Co/Fe**$_{0.2}$ samples a squared loop was measured while for the **Co/Fe**$_{0.6}$ this was not the case. The **Co/Fe**$_{0.6}$ sample had to be tilted significantly before a squared loop was obtained. This suggests that the easy axis and thus magnetization of the **Co/Fe**$_{0.6}$ sample has a significant *in-plane* component. Since out-of-plane magnetization of samples is required in order to be implemented in a synthetic ferromagnet the **Co**, **Co/Ni**, and **Co/Fe**$_{0.2}$ samples are selected to be further investigated with time-resolved measurements.

The difference in the results of the **Co/Fe**$_{0.2}$ and **Co/Fe**$_{0.6}$ samples can be explained by the theory in Section 2.1. Apparently, the thickness of the Fe layer in **Co/Fe**$_{0.6}$ was large enough as

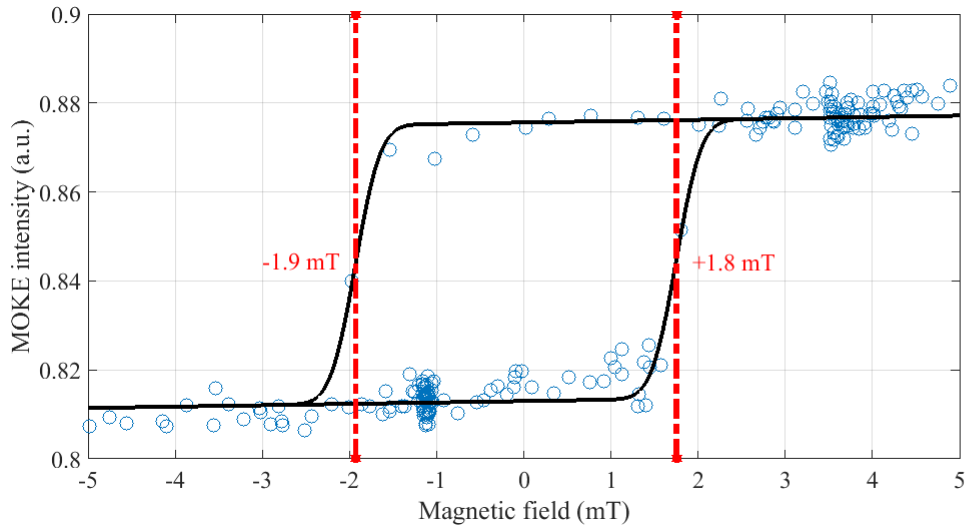


**Figure 4.2:** *The hysteresis loop of the* ***Co/Fe***$_{0.6}$ *sample as measurement by means of static MOKE. The sample was significantly tilted before a squared hysteresis loop could be measured, which implies that the easy axis not directed out-of-plane. The red dashed lines give the coercive field values. The data is fitted with equation 4.1.*

to make the total volume of the ferromagnetic part of this sample large enough for the volume anisotropy to dominate the surface anisotropy, which leads to in-plane magnetization. On the contrary, in the **Co/Fe**$_{0.2}$ sample the total volume of the ferromagnetic part stays small enough for the surface anisotropy to dominate. As previously mentioned this leads to out-of-plane magnetization.

If now one focuses on the hysteresis loops themselves an asymmetry can be perceived in the coercive field values. This asymmetry, as explained in Section 2.1, can be caused by the non-zero temperatures at which the MOKE measurements were performed as well as by incorrect magnet calibration. However, certain factors that regard how measurements are performed in general play a role too. Examples of these factors are the *rate* at which the applied magnetic field changes during the MOKE measurements as well as the *step size* with which these changes in the applied field are executed. Using smaller step sizes in general and a slower rate of change of the applied field for field values near $H_C$ not only lead to more data points and thus an improved fit but also to the sample being given more time to adjust to the applied field before it is increased again and thus to an increased accuracy in coercive field values. Yet, performing these measurements for low temperatures is crucial and in particular during measurements with a low rate of change in the field. The reason for this is that lower rates at higher temperatures give the thermal fluctuations opportunity to cause magnetization switching through processes other than by reaching the coercive field strength.

## 4.3 Time-resolved MOKE measurements

With the MOKE measurements having identified the samples with an out-of-plane magnetization the time-resolved measurements follow next. These TR-MOKE measurements are performed on the **Co**, **Co/Ni**, and **Co/Fe**$_{0.2}$ samples in order to determine the demagnetization times of these samples. If there appears to be a significant difference in demagnetization time between various samples, two of these samples can be incorporated within an earlier mentioned synthetic ferrimagnet

**Table 4.1:** *The parameters of the laser beam used for the TR-MOKE measurements.*

| | |
|---|---|
| Pulse length | 20 fs (output); $\sim$ 100 fs (at sample) |
| Wavelength | 700 nm |
| Repetition rate | 500 kHz |

that enables all-optical switching. For convenience, the **Co/Fe**$_{0.2}$ sample will from now on be called **Co/Fe**.

The time-resolved measurements were performed using the setup demonstrated in Figure 3.4. The characteristics of the laser are shown in Table 4.1. The PEM and chopper frequency were constant during every measurement at 42 kHz and 60 Hz, respectively. As mentioned in the previous chapter the probe and pump beam are focused on the same spot on the sample by means of the knife-edge method which is elaborated in Appendix A.

Before presenting the demagnetization curves obtained through the time-resolved measurements a process is elaborated through which the demagnetization curves will be scaled with respect to the maximum magnetization of the sample. A scaling factor is found by determining the demagnetization of a sample for a certain laser power and time delay ($t'$). This demagnetization is found by measuring the hysteresis loops without pump beam, i.e. no demagnetization of the sample has occurred, and with pump beam. Comparison of the step heights of the hysteresis loops with and without pump beam will give measure of the demagnetization for a certain laser power and time delay. More specifically, the demagnetization $D(t')$ is determined through

$$D(t') = 1 - \frac{|C_{\text{pump}}|}{|C_{\text{no pump}}|} \tag{4.2}$$

with $C_{\text{pump}}$ and $C_{\text{no pump}}$ corresponding to the fit parameter $C$ in equation 4.1 of the hysteresis with and without pump beam, respectively. As the time delay $t'$ and demagnetization $D(t')$ together represent a now known point on the demagnetization curve for a certain laser fluence the following formula can be used to scale the data $M_z$ with respect to the maximum magnetization $M_0$:

$$\frac{M_z}{M_0} = 1 - D(t') \cdot \frac{M_z}{|M_z(t')|}. \tag{4.3}$$

In case no data point is present on the known time delay $t'$ the mean is taken of the two magnitudes of magnetization with time delay values adjacent to $t'$. This mean will thus be used as an approximation for $M_z(t')$. An example of a pair of hysteresis loops is shown in Figure 4.3. These hysteresis loops were obtained for the **Co** sample for a laser fluence of 10.4 mJ/cm$^2$ while the time delay for the loop with pump was 1.59 ps. The results for the hysteresis measurements for other fluences of the **Co** sample as well those for the **Co/Ni** and the **Co/Fe** samples are placed in Appendix C.1.

About the results of the demagnetization measurements can be remarked in general that for increasing laser fluence the demagnetization increases. Intuitively this makes sense as for a higher laser fluence more heat is transferred to the sample leading to a decrease in magnetization of the ferromagnetic layers of the material and therefore to a decrease in the net magnetization of the sample.

As the scaling procedure has been clarified the results of the TR-MOKE experiments can now be discussed. The demagnetization curves are obtained by means of the setup showed in Figure 3.4. During these measurements the translation stage is used to incur various time delays to the pump and probe beams in order to pick up the signal at a different stage of the demagnetization process of the sample. In order to reduce the effects of signal noise averaging measurements is

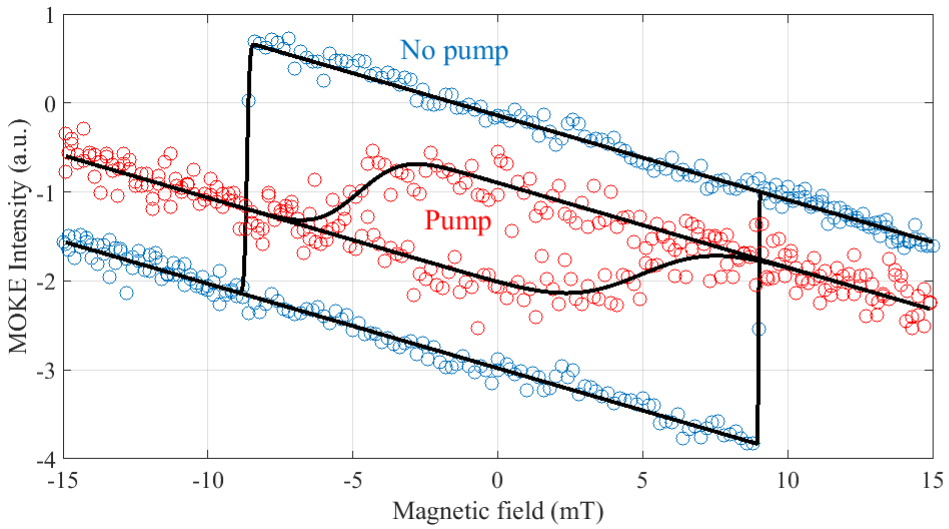


**Figure 4.3:** *Hysteresis loops of the* ***Co*** *sample with and without pump for a laser fluence of* $10.4\,mJ/cm^2$*. The loop with pump beam is obtained for* $t' = 1.59\,ps$ *corresponding to a demagnetization of* $60.6\%$*. The data is fitted with equation 4.1.*

crucial. Averaging the time-resolved measurements is achieved by applying a constant bias field perpendicularly to the sample surface as described earlier in section 3.2 and perform a series of measurements. Thereafter the bias field is reversed followed by a second series of measurements. Averaging is then achieved by binning the data point for positive and negative bias field separately. Subsequently the mean value is calculated of the data points within each bin as to obtain two averaged demagnetization curves, one for the positive, the other for the negative bias field. Finally, both curves are subtracted from one another which, after dividing by a factor two, delivers the average demagnetization curve. This final step removes the influence the bias fields have on the measurements.

The time-resolved experiments have been performed for various laser fluences and a bin size of 0.1 ps. An example of a set of averaged, yet unscaled, demagnetization curves for the **Co/Ni** using various laser fluences is depicted in Figure 4.4. On this figure can be seen how the magnetization of the sample experiences a larger drop for increasing laser fluence, which is consistent with the previous results of the hysteresis loops.

Before the demagnetization times of the samples can be determined, which is the aim of these time-resolved measurements, the experimental data (see Figure 4.4) has to be subjected to (i) scaling, (ii) fitting, and (iii) deconvolution. The scaling process has already been explained. The need for deconvolution originates from the fact that magnetization of the samples is measured by means of a Gaussian laser pulse. This pulse has a finite width in the time-domain and thus warps the response of magnetization of the sample after the absorption of a pump pulse. Deconvolution will correct this.

The fit function that is used for the demagnetization curves is based on a function presented in [22], which is the convolution of a Gaussian pulse and a response function. The response function is obtained by using the 3TM model to describe the demagnetization process, more specifically, the energy distribution among the spin, phonon, and electron systems after absorption of a laser pulse.

The convolution of the response function and the gaussian pulse is thus of the following form:

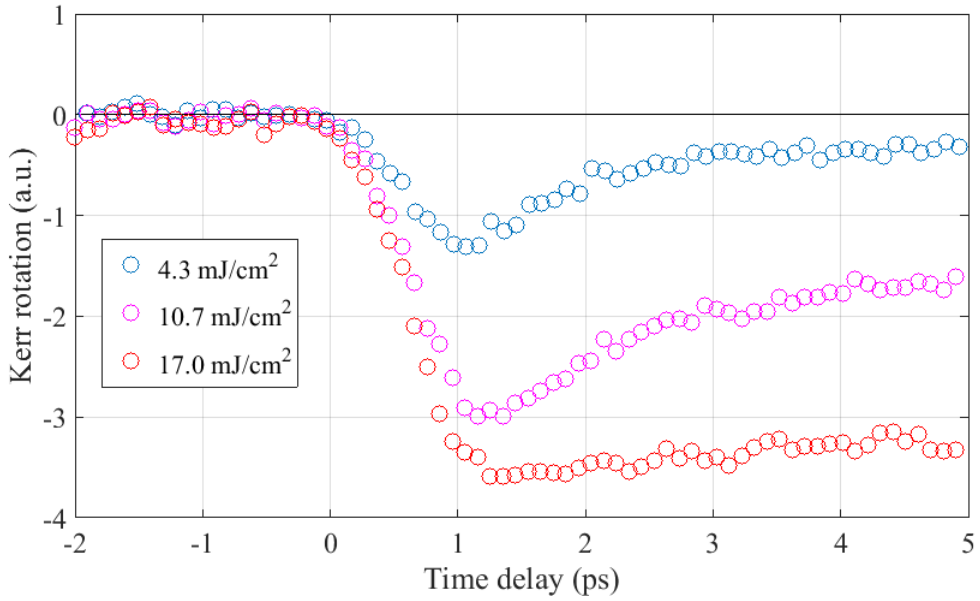


**Figure 4.4:** *Averaged, unscaled demagnetization curves of the* ***Co/Ni*** *sample obtained for a laser fluence of* 4.3, 10.7, *and* 17.0 $mJ/cm^2$.

$$
\begin{aligned}
y = {} & A_1 \frac{\operatorname{erf}\left(\frac{x-t_c}{s}\right)+1}{2\sqrt{\frac{x-t_c}{t_0}+1}} \\
& - \left(A_1 t_{\mathrm{mag}} - A_2 t_e\right) \exp\left\{\frac{s^2 - 4t_{\mathrm{mag}}\left(x-t_c\right)}{4t_{\mathrm{mag}}^2}\right\} \cdot \frac{1-\operatorname{erf}\left(\frac{s}{2t_{\mathrm{mag}}} - \frac{x-t_c}{s}\right)}{2\left(t_{\mathrm{mag}} - t_e\right)} \\
& - \left(A_1 - A_2\right) t_e \exp\left\{\frac{s^2 - 4t_e\left(x-t_c\right)}{4t_e^2}\right\} \cdot \frac{1-\operatorname{erf}\left(\frac{s}{2t_e} - \frac{x-t_c}{s}\right)}{2\left(t_e - t_{\mathrm{mag}}\right)} \\
& + A_3 \frac{\exp\left\{-\left(\frac{x-\mathrm{tc}}{s}\right)^2\right\}}{\sqrt{\pi}s} + A_4.
\end{aligned}
\tag{4.4}
$$

Herein $A_1$ to $A_4$, $t_0, t_c, t_e, t_{\mathrm{mag}}$, and $s$ are fit parameters used to manipulate the form of the function. Concerning these parameters it is important to keep in mind that they will not be used to determine the demagnetization time directly: the value of $t_{\mathrm{mag}}$ does not equal the demagnetization time. Ultimately, the respective form of the fit for the demagnetization curve is important and not the individual parameter values due to overparameterization of the fit function.

The results for the demagnetization curves of the **Co/Ni** sample are presented in Figure 4.5 while the results for the **Co** and **Co/Fe** samples are placed in Appendix C.2. The data has been scaled by means of equation 4.3 while a fit is obtained with equation 4.4. The fit clearly shows the initial dip in magnetization with a corresponding restoration over time periods much larger than 1 ps.

As mentioned before, the data fits are to be subjected to deconvolution in order to obtain the demagnetization times. For the **Co/Ni** sample this process has lead to the results shown in Figure

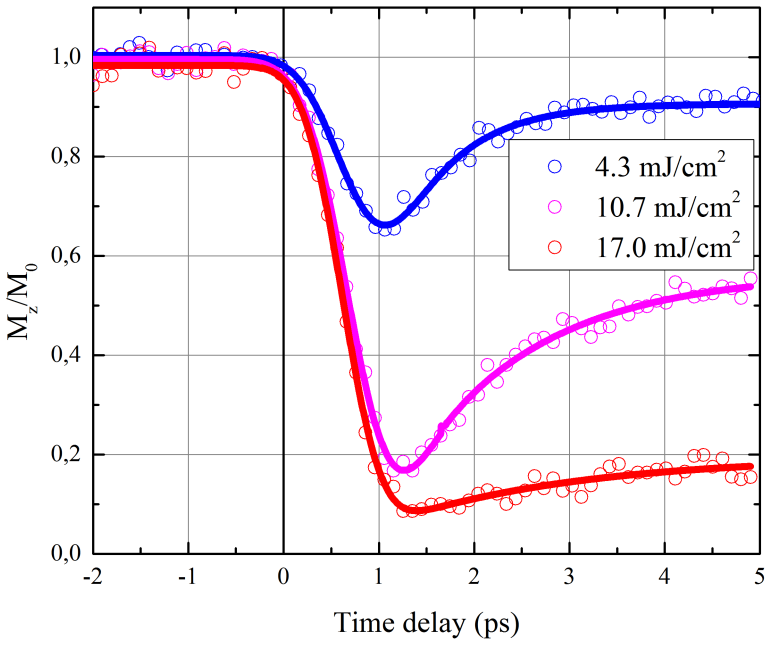


**Figure 4.5:** *Averaged, scaled demagnetization curves of the* ***Co/Ni*** *sample obtained for a laser fluence of* 4.3, 10.7, *and* 17.0 $mJ/cm^2$. *The used fit function is described in equation 4.4.*

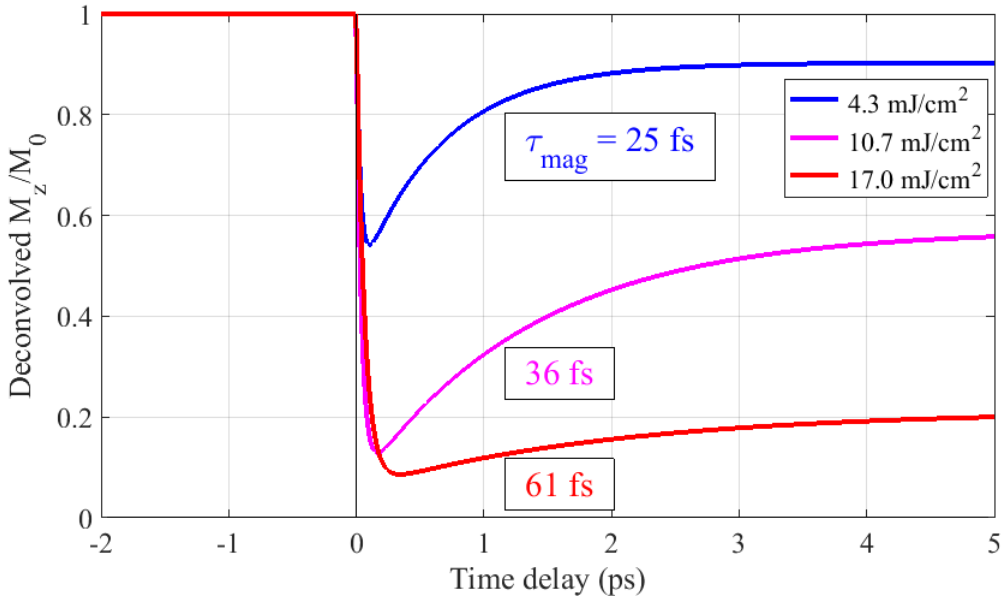


**Figure 4.6:** *The deconvolved demagnetization curves of the* ***Co/Ni*** *sample that are shown in Figure 4.5. The respective demagnetization times are given in the figure.*

4.6. The demagnetization times ($\tau_{\text{mag}}$) are given in the figure as well. The results for **Co** and **Co/Fe** samples are placed in Appendix C.2. The demagnetization times are determined by taking that time delay for which the magnetization has decreased to $1 - 1/e \approx 63.2\%$ of the total drop from maximum to minimum magnetization. The value of the demagnetization time is thus derived from this magnetization minimum.

Important to notice in Figure C.10 is that, although the demagnetization times consequently increase for increasing laser fluences, the curves of the two lower fluences with respect to that of the highest fluence are rather flat. The curves of the lower fluences should have a more clearly defined minimum. Prima facie this deviation in curve shape is characterized by the significantly differing fit parameter $t_c$ (equation 4.4) for various fluences. As this $t_c$ parameter signifies the width of the Gaussian pulse it should be constant for every laser fluence and sample as the experimental setup was not changed.

Overall the results reveal that the demagnetization times are in the order of tens of femtoseconds and that the demagnetization time as well as the maximum demagnetization increase for increasing laser fluence. The relation between the demagnetization time and the maximum demagnetization is depicted more clearly in Figure 4.7: a higher maximum demagnetization implies a larger demagnetization time. Noteworthy is also the presence of significantly more noise in the demagnetization measurements of the **Co** sample (see Figure C.9) compared to the **Co/Ni** and **Co/Fe** samples (Figures 4.5 and C.11, respectively). Unfortunately, the cause of this difference has remained unclear as the setup used for the **Co** sample was not different. It is possible that the sample itself was somehow damaged or that one or both the lock-in amplifiers were not optimally configured.

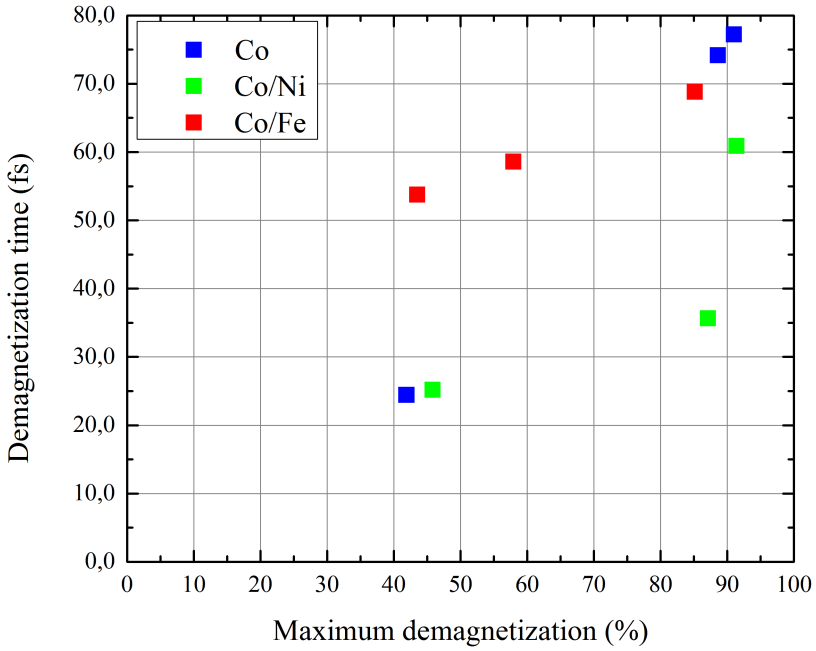


**Figure 4.7:** *The relation between the demagnetization time and maximum demagnetization. The demagnetization time increases for an increasing maximum demagnetization.*

In order to determine whether certain samples are compatible for integration into a synthetic

ferrimagnet it is necessary to compare the demagnetization times. As the synthetic ferrimagnet will be absorbing fs laser pulses which heat up the different layers in the sample equally, the demagnetization times of the samples integrated in the ferrimagnet have to significantly differ for the same laser fluence.

Comparison between the results of different samples starts by extracting from the deconvolved demagnetization curves the demagnetization times as a function of the laser power. Thereafter it is necessary to correct the results for (i) the repetition rate of the laser and (ii) a difference in laser spot size. This process is elaborated in Appendix D and entails a conversion from laser *power* into laser *fluence*. This conversion has been applied retroactively in the data mentioned above. The spot sizes used for the conversion have been determined through the *knife-edge method* (see Appendix A) while differences in the FWHM of the laser spot in y- and z-direction are averaged by taking the mean of the FWHM in both directions. The used spot size values are placed in Table D.1. Ultimately, applying the correction has resulted in the demagnetization time as function of the laser fluence as can be seen in Figure 4.8. The data shown in this figure is used for the selection of the samples suitable for enabling all-optical switching in a synthetic ferrimagnet.

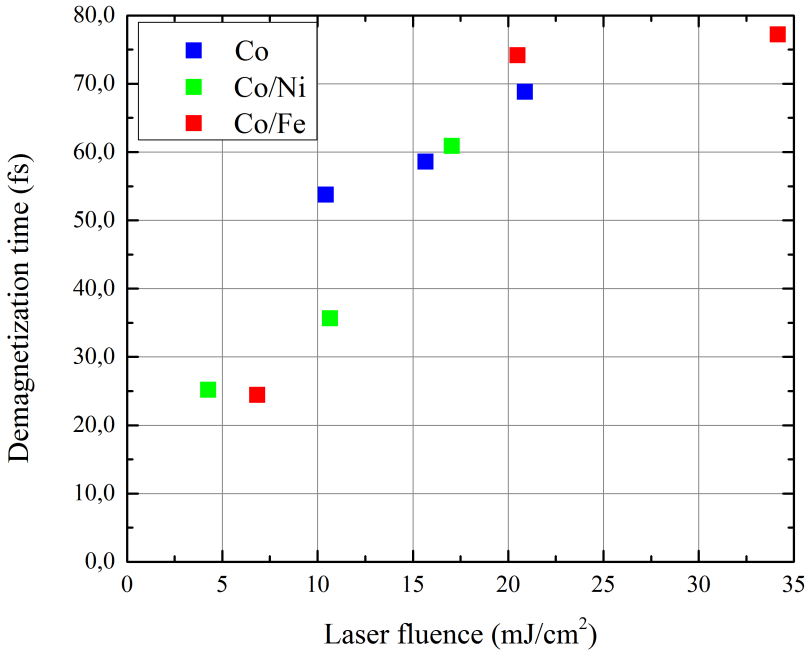


**Figure 4.8:** *The relation between the demagnetization time and laser fluence as obtained by using equation D.4.*

The most obvious option for integration within a synthetic ferrimagnet is the **Co** sample coupled with the **Co/Ni** sample while using a laser fluence of approximately 10 mJ/cm$^2$. The complete stack would thus be $Ta_{4.0}/Pt_{4.0}/\mathbf{Co}_{0.4}/Ru(d)/\mathbf{Co}_{0.3}/\mathbf{Ni}_{0.6}/\mathbf{Co}_{0.3}/Pt_{4.0}$ with the thickness $d$ of the non-magnetic spacer layer to be such as to antiferrimagnetically couple the two ferromagnetic layers. Concerning this conclusion several remarks can be made.

Firstly, there have not been made enough measurement covering the whole range of laser fluence in order to be able to compare the demagnetization time at more than a few points. The **Co/Ni**

or **Co/Fe** sample could, for instance, have been a good match with the **Co** sample if the results of the latter for a fluence of approximately $5\,\mathrm{mJ/cm^2}$ would have revealed a demagnetization time of several times larger than that of approximately 25 fs for the first two samples.

Furthermore, it is not even clear by how much the demagnetization times of the coupled layers have to differ for all-optical magnetic reversal to occur and if the laser fluence influences this difference in multiple. It is reasonable, however, to use the Fe/FePt bilayer simulations performed by Evans *et al.* [8] as a guideline. These simulations show that the demagnetization time of the slow layer (Fe) is at least *several multiples* that of the fast layer (FePt). Applying this result to the previous sample selection no couple of samples would be suitable within a synthetic ferrimagnet.

Finally, one can argue that an improvement in the reliability of the final results can be achieved by (i) an increase of the number of time-resolved measurements over which is averaged, (ii) a smaller resolution for the time-delay by an increased precision of the translation stage, (iii) using a smaller bin size during the averaging process, and (iv) measuring the demagnetization curves for a larger variety of laser fluences. Another option is to use different spots on the sample surface in order to be able to recognize and thus exclude damaged spots as these will give an anomalous signal. Lastly, it could be useful to take into account the real form of the laser spot instead of assuming it to be circular, especially if the radial size depends on the direction it is measured along.

# Chapter 5

# Conclusions and outlook

*This chapter first presents the conclusions of the experimental results described in this thesis. Afterwards a brief outlook will be given.*

## 5.1 Conclusions of experimental results

The static MOKE measurements revealed that the magnetization is directed *out-of-plane* for samples $Ta_{4.0}/Pt_{4.0}/\mathbf{Co}_{0.4}/Pt_{4.0}$, $Ta_{4.0}/Pt_{4.0}/\mathbf{Co}_{0.3}/\mathbf{Ni}_{0.6}/\mathbf{Co}_{0.3}/Pt_{4.0}$, and $Ta_{4.0}/Pt_{4.0}/\mathbf{Co}_{0.3}/\mathbf{Fe}_{0.2}/\mathbf{Co}_{0.3}/Pt_{4.0}$, while directed *in-plane* for sample $Ta_{4.0}/Pt_{4.0}/\mathbf{Co}_{0.3}/\mathbf{Fe}_{0.6}/\mathbf{Co}_{0.3}/Pt_{4.0}$. The time-resolved measurements are thus only performed on the first three samples. The difference between samples with the varying Fe thickness is a results of the volume anisotropy overcoming the surface anisotropy in $Ta_{4.0}/Pt_{4.0}/\mathbf{Co}_{0.3}/\mathbf{Fe}_{0.6}/\mathbf{Co}_{0.3}/Pt_{4.0}$ with an in-plane anisotropy as consequence. Noteworthy is the fact that during fabrication of the sample $Ta_{4.0}/Pt_{4.0}/\mathbf{Co}_{0.3}/\mathbf{Ni}_{0.6}/\mathbf{Co}_{0.3}/Pt_{4.0}$ complications occurred affecting the thickness of the lower non-magnetic parts of the sample. However, as the non-magnetic parts are sound, the measurements performed on this sample are still considered significant.

By means of the TR-MOKE experiments demagnetization times have been obtained which, after applying a correction for a difference in spot size, can be compared which each other. From this it was concluded that $Ta_{4.0}/Pt_{4.0}/\mathbf{Co}_{0.3}/\mathbf{Ni}_{0.6}/\mathbf{Co}_{0.3}/Pt_{4.0}$ sample seemed to be compatible with the $Ta_{4.0}/Pt_{4.0}$ $/\mathbf{Co}_{0.4}/Pt_{4.0}$ sample for a laser fluence of approximately $10\,\mathrm{mJ/cm^2}$. Ultimately, if simulations of Evans *et al.* are used as a guideline for how large the difference in demagnetization time of the two coupled layers should be, no couple of samples seems to be compatible at all for integration within a synthetic ferrimagnet. The simulations show the slow layer having a demagnetization time of several - up till ten - times larger than the fast layer, while in the experimental results the demagnetization time of a potential slow layer was at the most twice that of the corresponding fast layer. These conclusions should be perceived in an experimental context in which measurements were performed on every sample for only a limited amount of laser fluences.

## 5.2 Outlook

Although, as reported in [26], progress has been made on all-optical magnetic reversal in ferrimagnetic stacks containing gadolinium, switching behavior is not yet reported to have been occurring for a synthetic ferrimagnetic structure without gadolinium. That is, despite the concrete guidelines given in the limited amount of theoretical literature on this kind of ferrimagnet. As a result, if the use of gadolinium is regarded off limits, one is forced to use a trial and error approach in finding

suitable candidates that can be integrated into the synthetic ferrimagnet. Nevertheless a first suggestion can be to start using Fe as the slow switching layer as in the simulation paper [8] and then to go searching for a suitable fast switching layer. For this, variations on the structures mentioned in this thesis can be used, including incurring a difference in certain individual layers within each sample and the use of multilayers within a single ferromagnetic layer.

A second suggestion is using the fact that the amount of laser heat absorbed at a certain depth of the sample falls off exponentially. For the thinnest films this effect is small. However, as soon as film are used of much larger thickness, the thermal energy reaching the lower part of the synthetic ferrimagnet will be significantly lower than than reaching the upper part. The experimental results showed that the demagnetization time does indeed depend on the laser fluence, so the thickness could bring forth the necessary difference in demagnetization time to enable all-optical magnetic reversal. The question that now remaining is whether the difference in demagnetization time can be made large enough while keeping the amount of material necessary to fabricate the stack at a reasonable level.

# Bibliography


[1] Nicola A. Spaldin. *Magnetic Materials: Fundamentals and Applications*. Cambridge University Press, 2nd edition, 2010.

[2] Data storage statistics & facts. `https://www.statista.com/topics/3150/data-storage/`, (accessed 14-11-2017).

[3] S.N. Piramanayagam and C.C. Tow. *Developments in data storage: materials perspective*. IEEE, 1st edition, 2012.

[4] T.A. Ostler, J. Barker, R.F.L. Evans, R.W. Chantrell, U. Atxitia, O. Chubykalo-Fesenko, S. El Moussaoui, L. Le Guyader, E. Mengotti, L.J. Heyderman, F. Nolting, A. Tsukamoto, A. Itoh, D. Afanasiev, B.A. Ivanov, A.M. Kalashnikova, K. Vahaplar, J. Mentink, A. Kirilyuk, Th. Rasing, and A.V. Kimel. Ultrafast heating as a sufficient stimulus for magnetization reversal in a ferrimagnet. *Nat. Commun.*, 3(666):1–9, 2012.

[5] I. Tudosa, C. Stamm, A.B. Kashuba, F. King, H.C. Siegmann, J. Stöhr, G. Ju, B. Lu, and D. Weller. The ultimate speed of magnetic switching in granular recording media. *Nature*, 428:831–833, 2004.

[6] E. Beaurepaire, J.C. Merle, and J.Y. Bigot. Ultrafast spin dynamics in ferromagnetic nickel. *Phys. Rev. Lett.*, 76(22):4250–4253, 1996.

[7] C. D. Stanciu, F. Hansteen, A. V. Kimel, A. Kirilyuk, A. Tsukamoto, A. Itoh, and Th. Rasing. All-optical magnetic recording with circularly polarized light. *Phys. Rev. Lett.*, 99:047601, 2007.

[8] R.F.L. Evans, T.A. Ostler, R.W. Chantrell, I. Radu, and T. Rasing. Ultrafast thermally induced magnetic switching in synthetic ferrimagnets. *Appl. Phys. Lett.*, 104(8):082410, 2014.

[9] M. Ruderman and C. Kittel. Indirect exchange coupling of nuclear magnetic moments by conduction electrons. *Phys. Rev.*, 96:99–102, 1954.

[10] Kasuya T. A theory of metallic ferro- and antiferromagnetism on Zener's mode. *Prog. Thero. Phys.*, 16:45–57, 1956.

[11] K. Yosida. Magnetic properties of Cu-Mn alloys. *Phys. Rev.*, 106:893–898, 1957.

[12] M.L.M. Lalieu. Charging the interlayer exchange coupling. Master's thesis, Eindhoven University of Technology, 2017.

[13] A. Hubert and R. Schäfer. *Magnetic Domains: The Analysi of Magnetic Microstructures*. Springer, 3rd edition, 2009.

[14] M.J.G. Peeters. Domain-wall depinning using the precession torque. Master's thesis, Eindhoven University of Technology, 2016.

[15] M.T. Johnson, P.J.H. Bloemen, F.J.A den Broeder, and J.J. de Vries. Magnetic anisotropy in metallic multilayers. *Rep. Prog. Phys*, 59:1409, 1996.

[16] T.D. Cornelissen. Optical magnetic switching of ferromagnetic Co/Pt thin films. Master's thesis, Eindhoven University of Technology, 2015.

[17] E.C. Stoner and E.P. Wohlfarth. A mechanism of magnetic hysteresis in heterogeneous alloys. *IEEE Trans. Magn.*, 27:3475–3518, 1991.

[18] M.B. Agranat, S.I. Ashitkov, A.B. Granovskii, and G.I. Rukman. Interaction of picosecond laser pulses with the electron, spin, and phonon subsystems of nickel. *Zh. Eksp. Teor. Fiz.*, 86:1376–1379, 1984.

[19] A.J. Schellekens. *Manipulating spins: noval methods for controlling magnetization dynamics on the ultimate timescale*. PhD thesis, Eindhoven University of Technology, 2014.

[20] I. Radu, K. Vahapla, C. Stamm, T. Kachel, N. Pontius, H.A. Dürr, T.A. Ostler, J. Barker, R.F.L. Evans, R.W. Chantrell, A. Tsukamoto, A. Itoh, A. Kirilyuk, Th. Rasing, and A.V. Kimel. Transient ferromagnetic-like state mediating ultrafast reversal of antiferromagnetically coupled spins. *Nature*, 472:205–208, 2011.

[21] P. Weinberger. John Kerr and his effects found in 1877 and 1878. *Philosophical Magazine Letters*, 88(12):897–907, 2008.

[22] F.D. Longas. *Laser-induced magnetization dynamics: an ultrafast journey among spins and light pulses*. PhD thesis, Eindhoven University of Technology, 2008.

[23] E. Hecht. *Optics*. Pearson, 5th edition, 2016.

[24] C. You and Y. Shin. Derivation of simplified analytic formulae for magneto-optical Kerr effects. *Applied Physics Letters*, 69:1315–1317, 1996.

[25] W. Freeden and M. Gutting. *Special functions of mathematical (geo-)physics*. Birkhäuser, 2013.

[26] M. L. M. Lalieu, M. J. G. Peeters, S. R. R. Haenen, R. Lavrijsen, and B. Koopmans. Deterministic all-optical switching of synthetic ferrimagnets using single femtosecond laser pulses. *Phys. Rev. B*, 96, 2017.

[27] J.R. Taylor. *An introduction to error analysis*. University Science Books, 2nd edition, 1997.

# Appendix A

# Spot size determination and spatial overlap

In order to perform the TR-MOKE measurements it is necessary for the probe and pump beam to overlap, i.e. the centres of their laser spots coincide. Additionally, the spot size of the pump beam has to be small enough as to cause demagnetization of the sample while still being large enough to completely overlap the smaller probe beam.

As a rule of thumb, the ratio of the size of the pump and the probe are taken to be approximately 4 per spatial dimension (y- and z-direction), thus an area ratio of 16. The *knife-edge method* is used to achieve this. For practical reasons it is more convenient to start with the focusing of the probe beam while blocking the pump beam (the setup is depicted in Figure 3.4). Moving the sample along the x-direction, thus closer or further from the lens in front of it, alters the laser spot size.

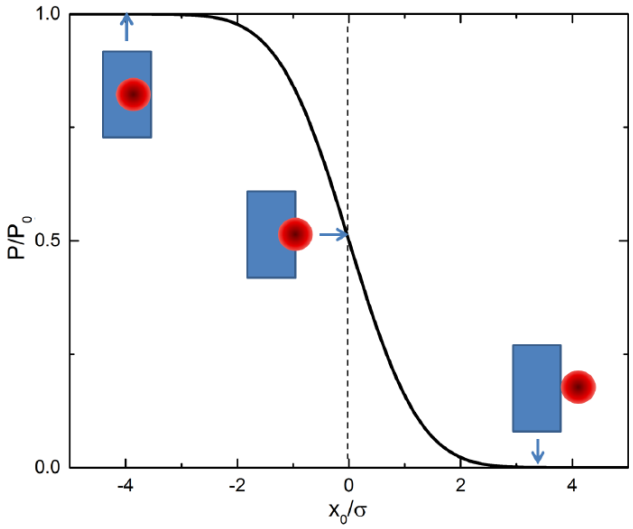


**Figure A.1:** *Example of a DC signal as obtained through the knife-edge method. From this curve the spot size and the spatial coordinate of the centre can be determined. Retrieved from [16].*

The knife-edge method requires to slowly vary the spatial coordinates of the sample, for constant x- and z-coordinates, from $(x_0, y_i, z_0)$ to $(x_0, y_f, z_0)$. If the y-coordinates $y_i$ and $y_f$ are chosen in such a way that for the first coordinate the laser spot is completely reflected by the sample while for

the second the sample does not fall on the sample at all, the detector will receive a DC signal similar to Figure A.1. This curve is then used to determine the spot size of the beam at this particular x-coordinate $x_0$ by fitting it with the *error function* of the form

$$A + B \operatorname{erf}(D(x - C)). \tag{A.1}$$

The resulting fit delivers the *full width at half maximum* (FWHM) as the width of the probe beam in the y-direction. Repeating the knife-edge measurements for the different x-coordinates $x_0$, reveals different curves and therefore a different spot size of the probe beam. Ultimately, a minimum spot size can be found for a certain x-coordinate $\tilde{x}$ which is used for future measurements. The value of the corresponding fit parameter $C$ functions as the y-coordinate $y_C$ of the probe beam centre.

Now that the spot size of the probe is determined, the probe beam is blocked and the pump is focused on the sample upon which the reflection is guided to the detector. The laser spot size of the pump beam is obtained by going through the similar steps as before, but now moving the sample from $(\tilde{x}, y_i, z_0)$ to $(\tilde{x}, y_f, z_0)$. A lens in the path of only the pump beam is thereafter used to alter the laser spot size until it has the desired width in y-direction. Finally, in order to cause overlap of both the probe and pump beam in y-direction, a mirror is used to move the pump beam in y-direction until the y-coordinate of the pump beam's centre $Y_C$ equals the probe beam's centre, i.e. $Y_C = y_C$.

Overlap in z-direction is achieved analogously to overlap in y-direction. However, now it is necessary, while keeping the x and y-coordinate constant, to vary the z-coordinate from $(\tilde{x}, y_0, z_i)$ to $\tilde{x}, y_0, z_f)$. The error function fit of the probe beam curve gives the centre's z-coordinate $z_C$ and spot size in z-direction, which should not deviate too much from the one in y-direction. Now, similar edge measurements are done with the pump beam until they also overlap in z-direction, i.e. $Z_C = z_C$.

# Appendix B

# Results static MOKE measurements

In this appendix the remaining results are presented of the static MOKE measurements done on the **Co/Ni** and **Co/Fe**$_{0.2}$ samples. These results imply an *out-of-plane* magnetization for both samples.

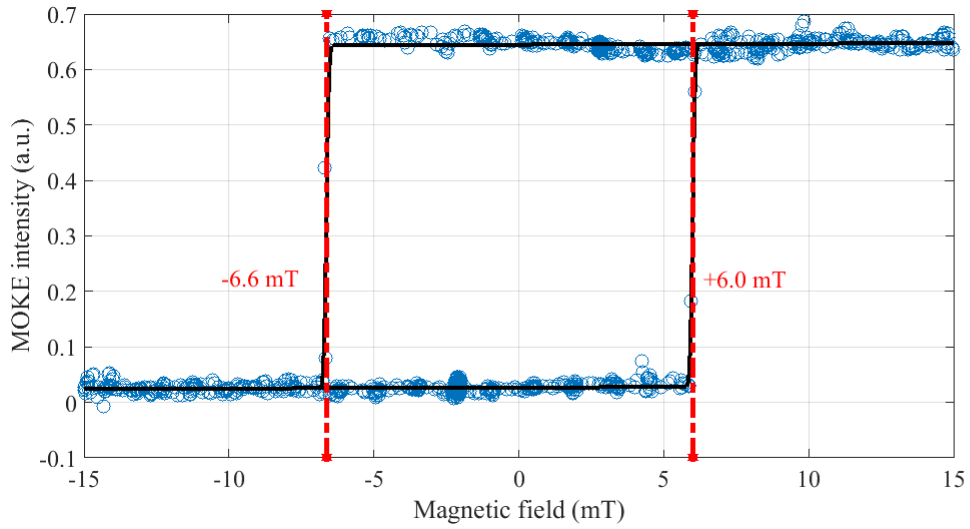


**Figure B.1:** *The hysteresis loop of the **Co/Ni** sample as measured by means of polar MOKE. The squared shape of the loop indicates that the magnetization of the sample is directed out-of-plane. The red dashed lines give the coercive field values. The data is fitted with equation 4.1.*

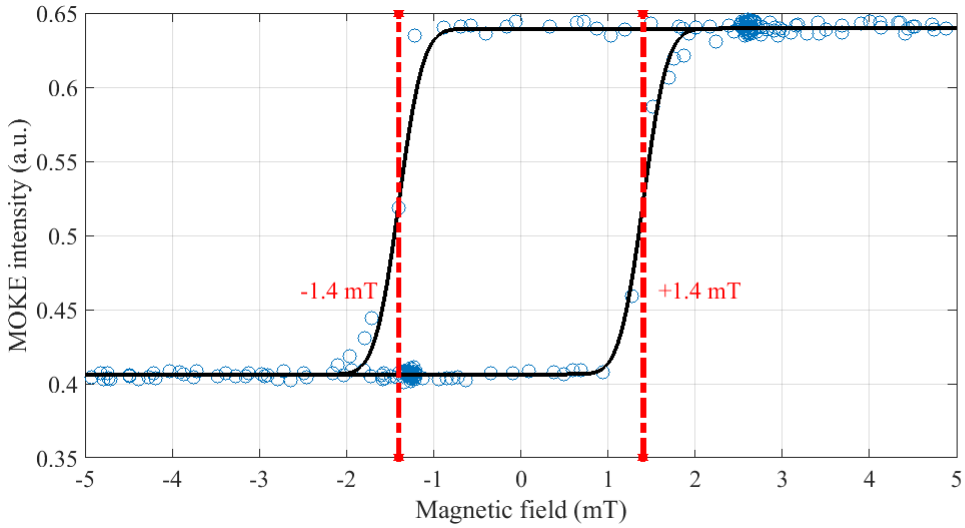


**Figure B.2:** *The hysteresis loop of the* $\boldsymbol{Co/Fe_{0.2}}$ *sample as measured by means of polar MOKE. The squared shape of the loop indicates that the magnetization of the sample is directed out-of-plane. The red dashed lines give the coercive field values. The data is fitted with equation 4.1.*

# Appendix C

# Results time-resolved measurements

## C.1 Hysteresis loops with and without pump beam

In this section the remaining results of the hysteresis measurements with and without pump beam are shown for various laser fluences. It was only necessary to do these measurements on the **Co**, **Co/Ni**, and **Co/Fe**$_{0.2}$ samples. The pairs of hysteresis loops are used to determine the demagnetization of the samples for a certain time delay which is used to scale the time-resolved measurements for the corresponding laser fluence.

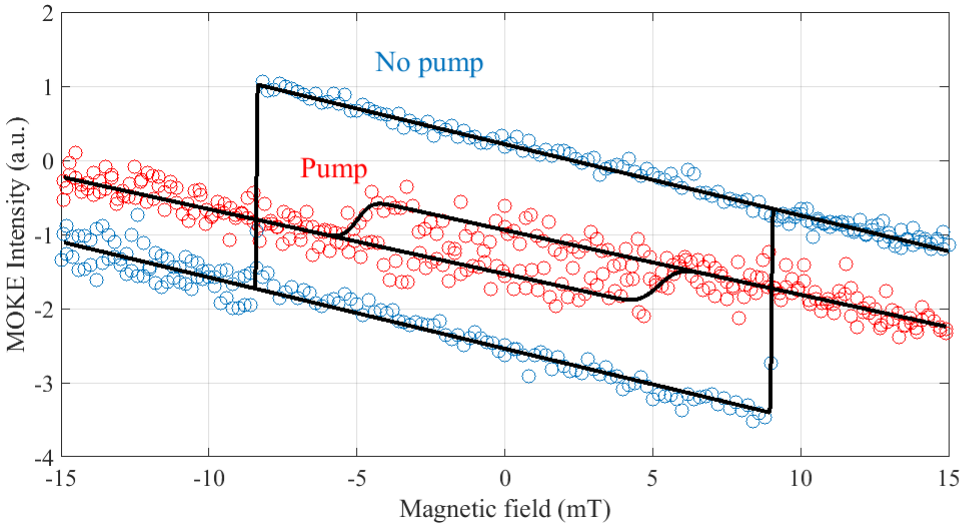


**Figure C.1:** *Hysteresis loops of the **Co** sample with and without pump for a laser fluence of* 15.7 $mJ/cm^2$ *corresponding to a demagnetization of* 78.5%. *The loop with pump beam is obtained for a time delay of* 1.59 *ps. The data is fitted with equation 4.1.*

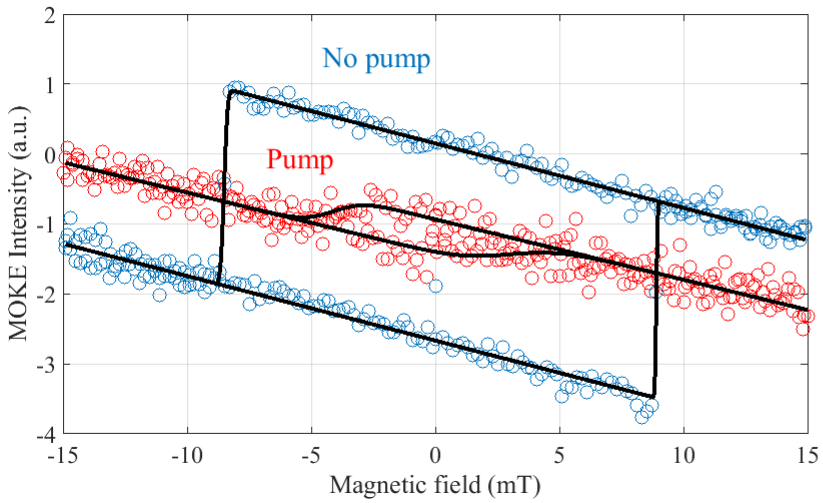


**Figure C.2:** *Hysteresis loops of the* ***Co*** *sample with and without pump for a laser fluence of* $20.9\,mJ/cm^2$ *corresponding to a demagnetization of* $82.9\%$*. The loop with pump beam is obtained for a time delay of* $1.59\,ps$*. The data is fitted with equation 4.1.*

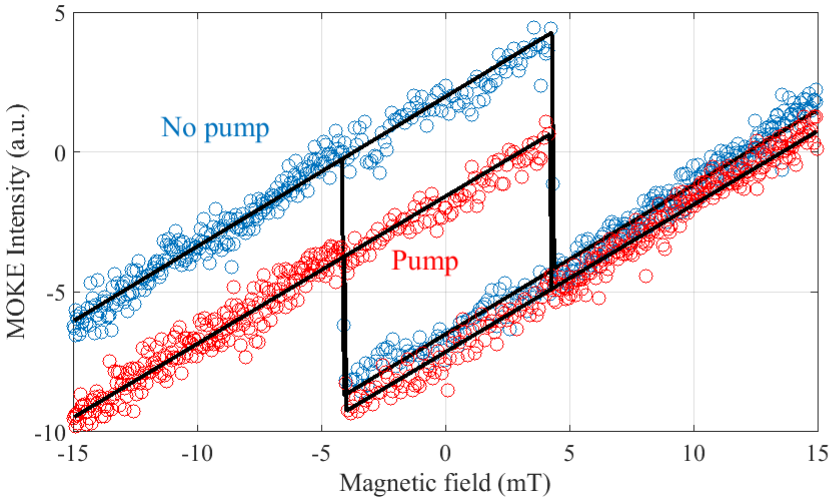


**Figure C.3:** *Hysteresis loops of the* ***Co/Ni*** *sample with and without pump for a laser fluence of* $4.3\,mJ/cm^2$ *corresponding to a demagnetization of* $34.5\%$*. The loop with pump beam is obtained for a time delay of* $1.00\,ps$*. The data is fitted with equation 4.1.*

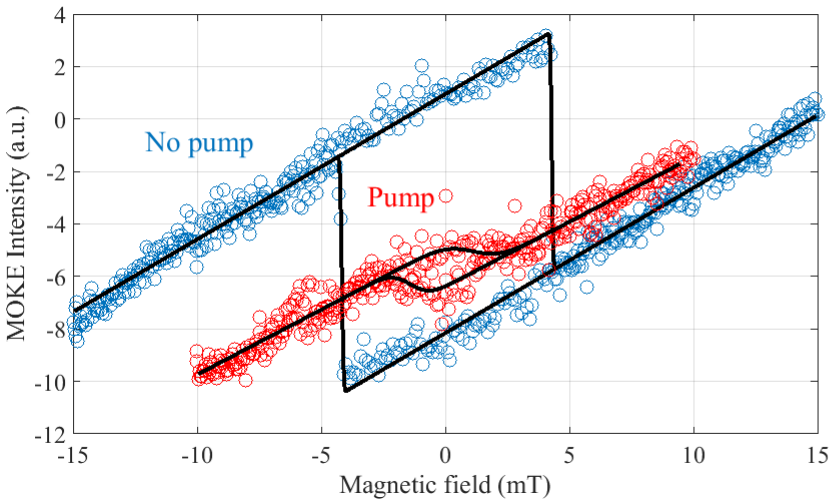


**Figure C.4:** *Hysteresis loops of the* ***Co/Ni*** *sample with and without pump for a laser fluence of* $10.7\,mJ/cm^2$ *corresponding to a demagnetization of* $82.4\%$*. The loop with pump beam is obtained for a time delay of* $1.29\,ps$*. The data is fitted with equation 4.1.*

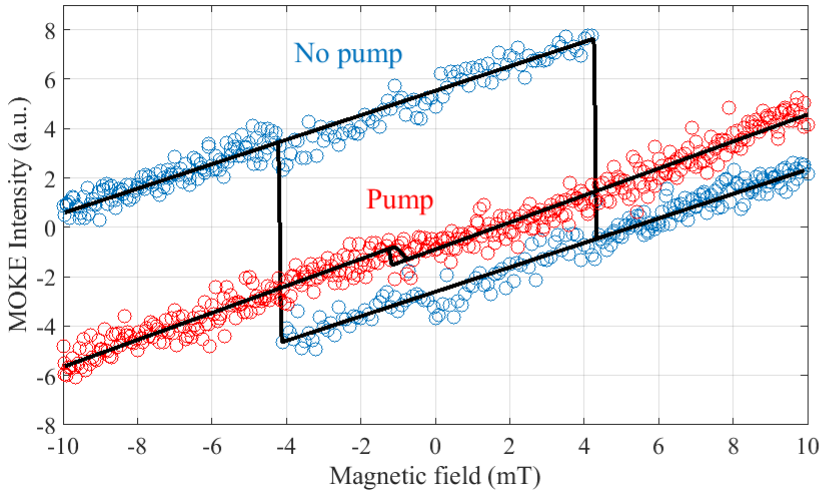


**Figure C.5:** *Hysteresis loops of the* ***Co/Ni*** *sample with and without pump for a laser fluences of* $17.0\,mJ/cm^2$ *corresponding to a demagnetization of* $91.4\%$*. The loop with pump beam is obtained for a time delay of* $1.29\,ps$*. The data is fitted with equation 4.1.*

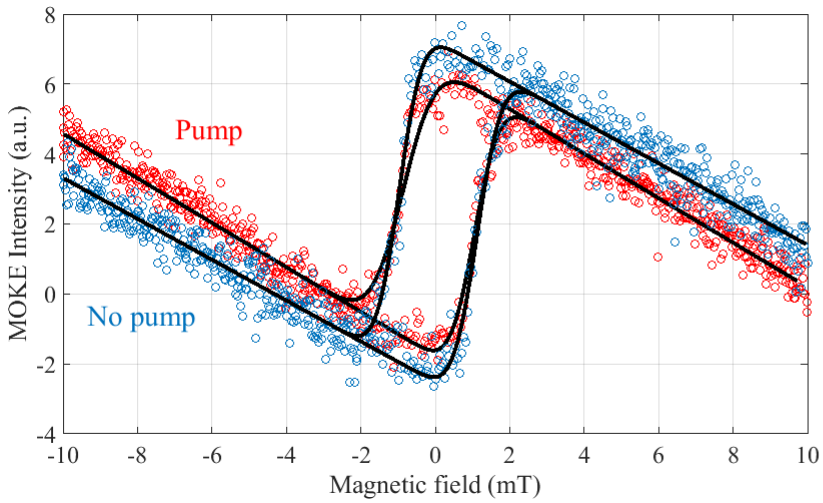


**Figure C.6:** *Hysteresis loops of the* ***Co/Fe*** *sample with and without pump for a laser fluence of* $6.8\,mJ/cm^2$ *corresponding to a demagnetization of* $14.6\%$*. The loop with pump beam is obtained for a time delay of* $5.00\,ps$*. The data is fitted with equation 4.1.*

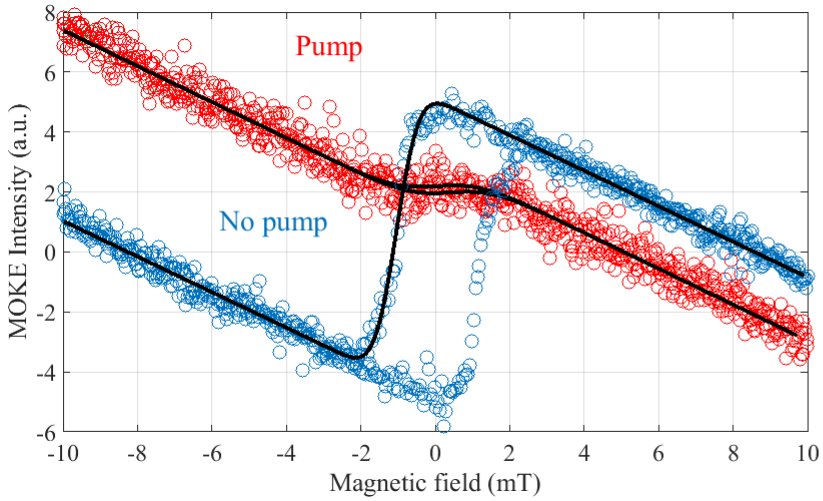


**Figure C.7:** *Hysteresis loops of the* ***Co/Fe*** *sample with and without pump for a laser fluence of* $20.5\,mJ/cm^2$ *corresponding to a demagnetization of* $83.7\%$*. The loop with pump beam is obtained for a time delay of* $5.00\,ps$*. The data is fitted with equation 4.1.*

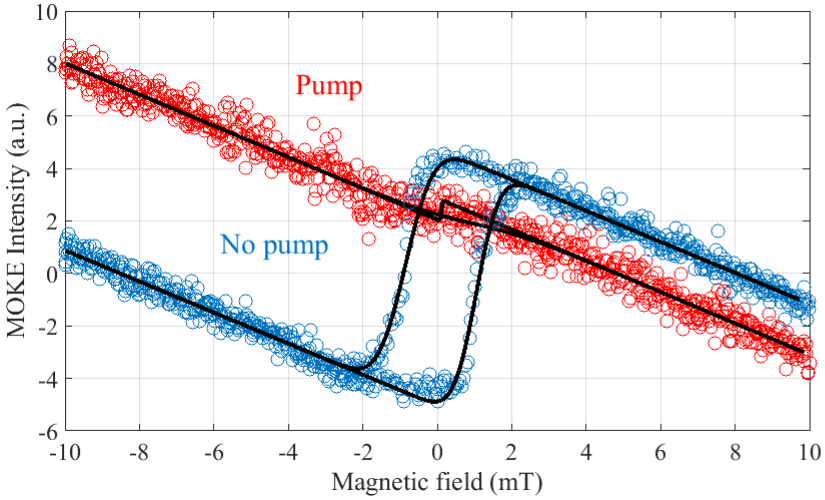


**Figure C.8:** *Hysteresis loops of the* ***Co/Fe*** *sample with and without pump for a laser fluence of* $34.2\,mJ/cm^2$ *corresponding to a demagnetization of* $91.6\%$*. The loop with pump beam is obtained for a time delay of* $5.00\,ps$*. The data is fitted with equation 4.1.*

## C.2 Demagnetization curves

In this section the demagnetization curves of the **Co** and **Co/Fe** samples are presented. First the experimental data is shown with a corresponding fit after which the deconvolved fit is presented.

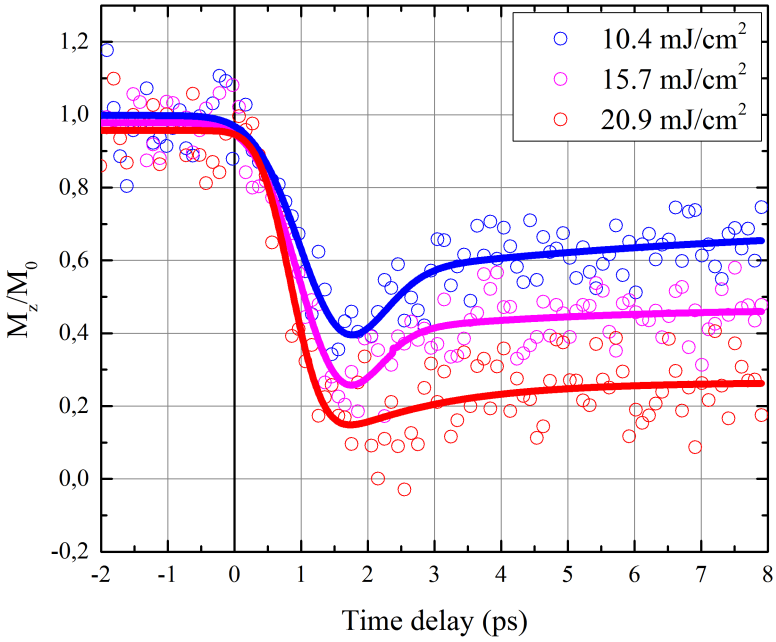


**Figure C.9:** *Averaged, scaled demagnetization curves of the **Co** sample obtained for a laser fluence of* 10.4, 15.7, *and* 20.9 $mJ/cm^2$. *The used fit function is described in equation 4.4.*

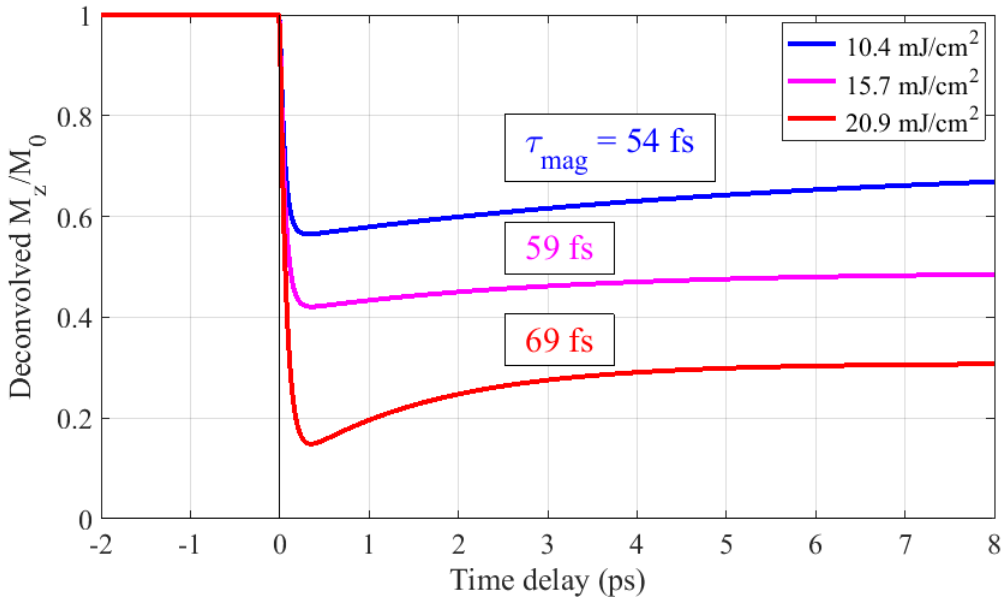


**Figure C.10:** *The deconvolution of the demagnetization curves of the **Co** sample that are shown in Figure C.9. The respective demagnetization times are given in the figure.*

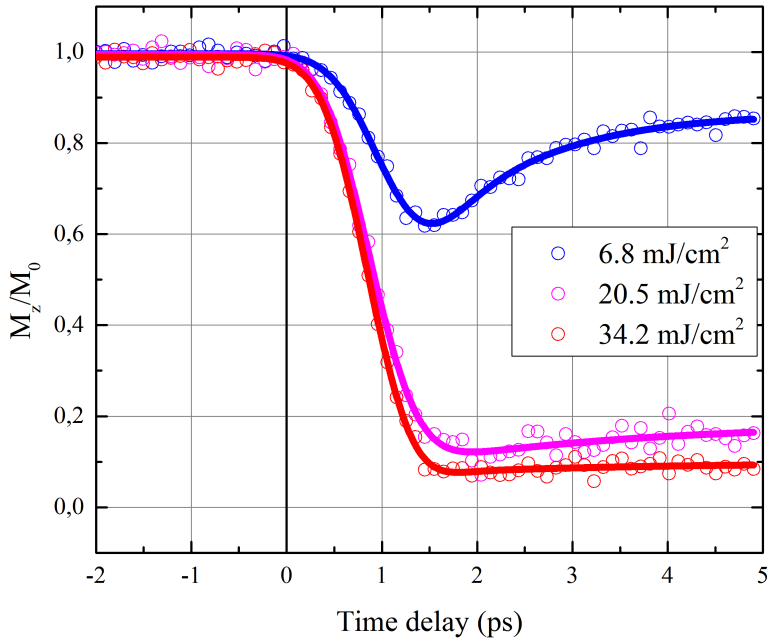


**Figure C.11:** *Averaged, scaled demagnetization curves of the **Co/Fe** sample obtained for a laser fluence of 6.8, 20.5, and 34.2 $mJ/cm^2$. The used fit function is described in equation 4.4.*

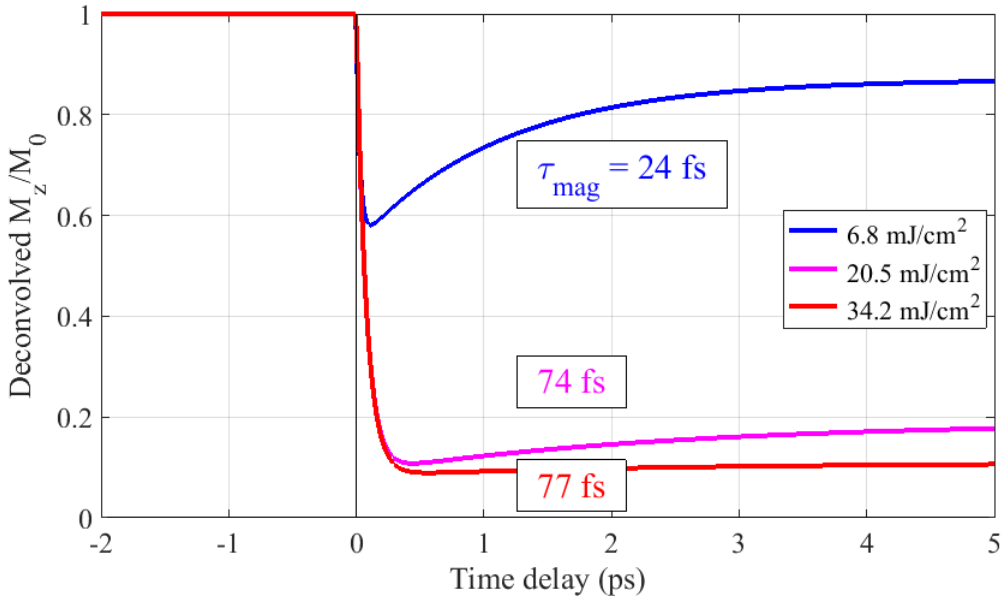


**Figure C.12:** *The deconvolution of the demagnetization curves of the* ***Co/Fe*** *sample that are shown in Figure C.11. The respective demagnetization times are given in the figure.*

# Appendix D

# Conversion from laser power into laser fluence

The conversion from laser *power* ($\mathcal{P}$) to laser *fluence* ($\mathcal{F}$) is made by involving the *repetition rate* $f$ and the *spot size* $A$ of the laser. The laser used for the TR-MOKE measurements has a repetition rate of 500 kHz. The spot size can be determined by assuming a *2D Gaussian intensity profile* of the form

$$I(y,z) = I_0 \exp\left(-\frac{y^2+z^2}{2\sigma^2}\right) \tag{D.1}$$

wherein $I_0$ is the peak intensity and $\sigma$ is a measure of the beam width. However in this project the beam width and thus the spot size is instead chosen to be determined by the *full width at half maximum* (FWHM) which is related to $\sigma$ through [27]

$$\text{FWHM} = 2\sqrt{2\ln 2}\,\sigma \approx 2.335\,\sigma. \tag{D.2}$$

The spot size is thus be determined by

$$A = \pi\left(\frac{\text{FWHM}}{2}\right)^2. \tag{D.3}$$

Finally, the laser fluence can be calculated by

$$\mathcal{F} = \frac{\mathcal{P}}{f \cdot A} = \frac{\mathcal{P}}{\pi f}\left(\frac{2}{\text{FWHM}}\right)^2 = \frac{4\mathcal{P}}{\pi f \text{FWHM}^2}. \tag{D.4}$$

**Table D.1:** *The spot sizes in y- and z-direction, i.e. $FWHM_y$ and $FWHM_z$, respectively, are averaged, so $FWHM = (FWHM_y + FWHM_z)/2$. Hereupon equation D.3 is used to determine the spot size A.*

| | $\text{FWHM}_y$ ($\mu$m) | $\text{FWHM}_z$ ($\mu$m) | $A$ ($\mu\text{m}^2$) |
|---|---|---|---|
| **Co** | 71.1 | 68.6 | 3832 |
| **Co/Ni** | 81.3 | 73.3 | 4693 |
| **Co/Fe$_{0.2}$** | 41.2 | 80.9 | 2927 |